Gingerbread ingredient-derived carbons-assembled CNT foam for the efficient peroxymonosulfate-mediated degradation of emerging pharmaceutical contaminants

Tam Do Minh[a,*], Mohamed Chaker Ncibi[a], Varsha Srivastava[a], Senthil Kumar Thangaraj[b], Janne Jänis[b], Mika Sillanpää[a,c,*]

[a] Department of Green Chemistry, School of Engineering Science, Lappeenranta University of Technology, Sammonkatu 12, FI-50130 Mikkeli, Finland
[b] Department of Chemistry, University of Eastern Finland, P.O. Box 111, FI-80101 Joensuu, Finland
[c] Department of Civil and Environmental Engineering, Florida International University, Miami, FL, 33174, USA
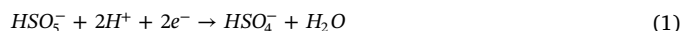
ARTICLE INFO

ABSTRACT

This article reports on the macronization of self-supported 3D CNT foam inter-connected by heteroatom-enriched porous shells derived from renewable baking ingredients via mild pyrolysis. The synthesized hybrids enabled disintegrating peroxymonosulfate (PMS) into reactive oxidants (sulfate radicals, hydroxyl radicals, and singlet oxygen) for the degradation of atenolol, iopamidol, metformin, trimethoprim, and phenol in water. Hierarchically structured nitrogen- and oxygen-doping significantly enhanced adsorptive and catalytic performance whereas the magnetic 3D framework promoted mass transport, multicycle use and induced synergetic effects via the Me-N$_x$-C interfaces. The samples were highly efficient for degradative removal of model pollutants at low catalyst and PMS dose. The catalyst loading, PMS dose, contact time, and temperature positively influenced the removal potency while pH and water matrix governed the rates differently. Spin trapping, oxidant quenching and solvent isotope effect study coupled with liquid chromatography and Fourier transform ion cyclotron resonance mass spectrometry analysis suggested the footprints of transformation products via a dual-mode (radical and non-radical) activation of PMS. This durable, magnetic carbofoam might be a promising catalyst for the oxidative abatement of pharmaceutical micropollutants from contaminated waters.

1. Introduction

The increasing degradation of water quality by anthropogenic pollutants is threatening human wellbeing and ecosystem sustainability [1,2]. Pharmaceutical active compounds (PhACs) are among the most persistent and toxic aqueous pollutants, demanding the application of hybrid technologies for effective abatement [3]. Many PhACs passed through conventional decontamination processes unchanged or in the forms of harmful metabolites and transformation products (TPs) [3,4]. The biological activity at ultra-trace quantities will have potential effects on the human and environment health unless remediation approaches succeed in decomposing PhACs to inert end-products [5].

Advanced oxidation processes (AOPs) have been explored as a promising choice for oxidative abatement of organic micropollutants [6–11]. Under that canopy, peroxymonosulfate (PMS)-mediated oxidative destruction offers great prospects and potency, having high

oxidative potential (2.5–3.1 eV) and a long half-life (30–40 μs) of sulfate radical [6,9]. Carbon nanotubes (CNTs) have been the focus of considerable recent attention as metal-free PMS-activators, able to generate resilient oxidizing species (Eqs. (1)–(4)) for the complete mineralization of organic pollutants [12–17]:

$$HSO_5^- + 2H^+ + 2e^- \rightarrow HSO_4^- + H_2O \tag{1}$$

$$HSO_5^- + e^- \rightarrow {}^\bullet OH + SO_4^{2-} \tag{2}$$

$$HSO_5^- + e^- \rightarrow OH^- + SO_4^{\bullet -} \tag{3}$$

$$2SO_5^{2-} \rightarrow {}^1O_2 + 2SO_4^{2-} \tag{4}$$

Although disintegrating PMS into hydroxyl radical (${}^\bullet OH$) and singlet oxygen (${}^1O_2$) can be manipulated by tuning catalyst properties, numerous efforts have been devoted to developing carbon-sourced catalysts for sulfate radical-mediated AOPs [17–26]. Among those,

---

heteroatom-doped sp^2-hybridized carbons have shown excellent potency (Eqs. (5)–(7)) [27].

$$C \cdots \pi^+ + HSO_5^- \rightarrow C \cdots \pi + OH^- + SO_4^{\bullet-} \quad (5)$$

$$C = C = N + HSO_5^- \rightarrow C = C = N^+ + OH^- + SO_4^{\bullet-} \quad (6)$$

$$C = C = O + HSO_5^- \rightarrow C = C = O^+ + OH^- + SO_4^{\bullet-} \quad (7)$$

Tailoring both structural and compositional features of carbocatalysts has emerged as a very effective strategy to fine-tune activation power. Recently, Shao et al. proposed that ketonic carbonyl on nanodiamonds facilitated PMS decomposition to $^1O_2$ for rapid oxidation of phenolic compounds (Eqs. (8)–(9)) [28].

$$HSO_5^- - e^- \rightarrow H^+ + SO_5^{\bullet-} \quad (8)$$

$$2SO_5^{\bullet-} \rightarrow {}^1O_2 + S_2O_8^{2-} \quad (9)$$

In comparison to pristine 0D nanodiamonds, 1D CNTs, and 2D graphene, their heteroatom-doped derivatives have demonstrated enhanced catalytic activity towards PMS [9,10,17]. Although encouraging degradation has been shown for various model compounds, substantial loss in activity and low reusability remain major disadvantages. Particularly, synthetic heteroatom-doped CNTs have on their outer plain carbon active moieties vulnerable to oxidation and dissolved organic matter [7], causing deterioration of functionality and eventually deactivation [12,13,17]. Due to the inertness of the basal surface, a modification strategy relying solely on loading dopant precursors may not achieve adequate intrinsic change in structure and reactivity [23]. The in-situ development of heteroatom-functionalized protective shells for synergistic effect and long durability is thus imperative in this regard.

Carbon-sourced activators with low metal footprint are critical for cost-effective and greener water remediation using PMS-mediated AOPs. However, energy-intensive ultrafiltration is necessary to recover the nanoparticles thus eliminating the risks of secondary pollution [29]. The potential effects of CNTs on human health and the ecosystem pose concerns against the practical use of its suspensions in water purification [30–32]. To overcome this implementation barrier [33], assembling CNTs into macroscopic architecture for packed-bed reactors or smart catalytic devices would be an alternative and environmentally benign solution [7,34–37]. Although different heteroatom-doped carbocatalysts have been intensively examined [18–28,35–43], the fabrication and efficacy of freestanding CNT foam@PMS system for pharmaceutical abatement have not been reported, making its exploitation of great importance.

The past decade has witnessed a tremendous increase in global concern and awareness about the sources, the occurrence, and the fate of emerging PhACs contaminants in aquatic environments [44–46]. Recent studies have demonstrated that AOPs can substantially degrade some representative compounds including atenolol [47,48], trimethoprim [49,50], metformin [51], and iopamidol [52–58]. Considering global consumption [59–61], persistent toxicity [62–65], and the structural diversity of these PhACs, their behavior in CNT-based carbocatalyst@PMS system was expected to be critically representative and needs to be urgently examined.

Keeping the above in mind, the current study adopted a simple, scalable pyrolysis strategy to fabricate macroscopic CNTs-based catalysts for PMS-mediated AOPs. Heteroatom-rich shells derived from renewable baking ingredients (glucose, citric acid and ammonium carbonate) assembled a CNT skeleton onto free-standing functionalized hierarchical porous hybrids. The residual catalysts (Fe$_3$C, Fe, and Co) present in the tubules interact with the N-rich carbon layers, forming a diversity of active interfaces to enhance the overall catalysis [15–17,37–43,66–70]. Meanwhile, with a coating of tunable thickness adhering to tubule surface, the hybrids presented a large surface area, had good thermal stability, preserved magnetic feature, and facilitated multicycle stability. Due to the synergistic effect of doped heteroatoms,

structural defects, and 3D network-supported diffusion, the catalytic potency and durability were markedly boosted compared to the pristine CNTs, Fe$_3$O$_4$, and other selected reference materials. Several operating parameters were varied, and their impact on degrading four PhACs at high concentrations (10 to 40 mg/L) were evaluated. Electron paramagnetic resonance (EPR) spin trapping, solvent isotope effect and quenching study suggested a dual-mode activation mechanism of PMS. Liquid chromatography coupled with Fourier transform ion cyclotron resonance mass spectrometry (FTICR-MS) analysis revealed transformation products and plausible degradation pathways were proposed. The present work demonstrates the efficient use of 3D free-standing magnetic CNTs-based catalysts for the effective degradation of emerging PhACs in contaminated waters.

2. Experimental

2.1. Materials and chemicals

Atenolol, trimethoprim, metformin hydrochloride, iopamidol, D-glucose, citric acid, ammonium carbonate, peroxymonosulfate (KHSO$_5$.½KHSO$_4$.½K$_2$SO$_4$, Oxone®), single-walled CNTs (lot# 805033, L: > 5 μm, diameter: 1.3–2.3 nm), 2,2,6,6-tetramethyl-piperidine were purchased from Sigma Aldrich. 5,5-dimethyl-1-pyrroline was obtained from Fluka. The pristine CNTs (p-SW) were purified by 3 M HCl to give pu-SW. The molecular descriptor values for tested compounds is presented in Table S1 (Supporting Information).

2.2. Catalyst preparation

This method was adapted from Liu et al. with minor modification [35]. Briefly, p-SW (0.5 g) was mixed with a pre-grounded mixture of D-glucose (1 g), ammonium carbonate (1 g), and citric acid (0.7 g). Glucose and citric acid were used as scaffolder and O-dopant; ammonium carbonate acted as "gas template" and N-precursor. CNTs were introduced to form a skeleton for the scaffold. Different hybrids were prepared by varying the mass of citric acid (0.7–3.5 g), annealing temperature (450–700 °C), and holding time (1–12 h). The as-obtained materials were washed with 1 M HCl followed by copious water and ethanol then dried at 105 °C. Scheme 1 illustrates the evolution of precursors upon heat treatment on a p-SW substrate. The preparation of all materials is presented in the Supporting Information and is summarized in Table 1.

2.3. Catalyst characterization

The surface morphology was observed with an FE-SEM (Hitachi SU3500) and TEM (Hitachi 7700). Thermo-gravimetric analysis was performed using a Perkin Elmer TGQ500 system at 25–900 °C in air. Surface functionalities and chemistry were characterized with an FTIR (Bruker, Vertex 70) and an ESCALAB 250 XPS system. N$_2$ sorption measurements were performed at 77 K using a Micromeritics Tristar II Plus; Brunauer-Emmett-Teller (BET) and Barrett-Joyner-Halenda (BJH) methods were used to estimate the specific surface area, pore volume and pore size distribution, respectively. The total pore volume (V$_t$) was obtained at relative pressure p/p$_0$ = 0.90. XRD diffraction patterns were collected using PANalytical equipment. Raman spectroscopy was studied using a Horiba Jobin Yvon, Labram HR microscope equipped with a 513.4 nm laser.

2.4. Experimental procedure

Unless otherwise specified, experiments were performed at 25 ± 2 °C in open flasks containing 500 mL solutions of PhACs (10 mg/L, native pH), carbofoam (0.1 g/L) with or without PMS (1 g/L). Periodically, a magnet was used to isolate the catalyst and 1.0 ml filtrate aliquot (0.2 μm syringe filter) was sampled into glass vial, which,
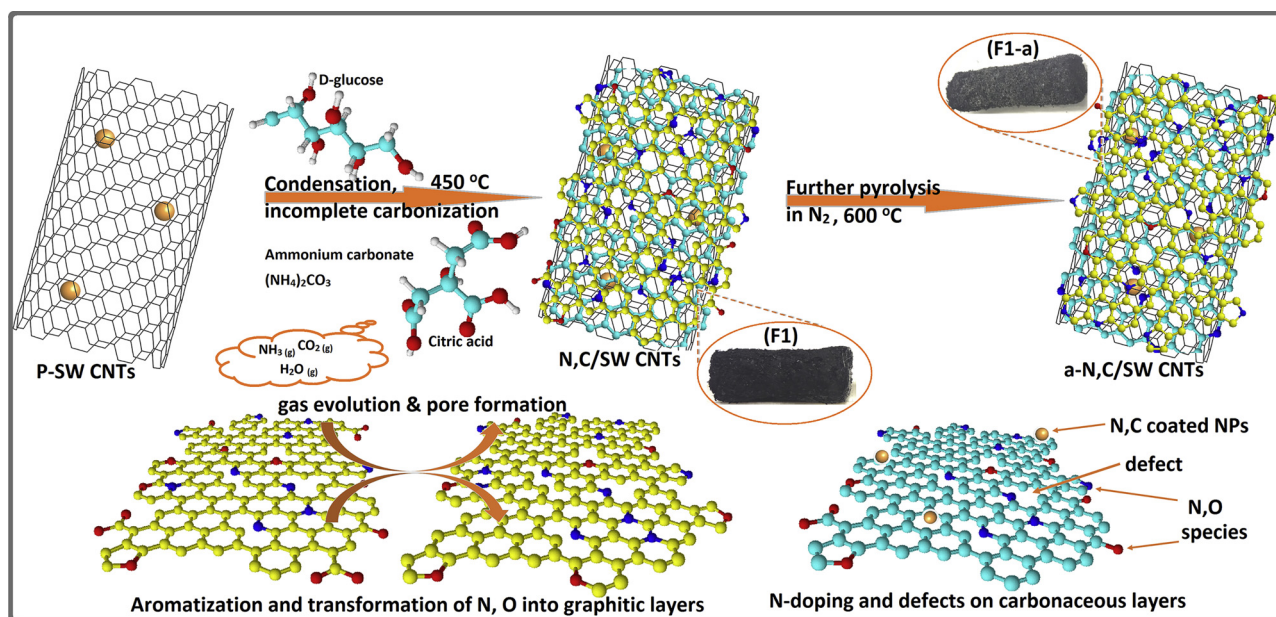
Scheme 1. Illustrative evolution of carbonaceous layers on SWCNTs substrate.

in case of oxidation tests, was pre-filled with 0.5 ml methanol to quench the excessive reactive species. The concentrations of PhACs were quantified using a high-performance liquid chromatography system (HPLC, Shimadzu), and Fourier transform ion cyclotron resonance (FT-ICR) mass spectrometry (12-T Bruker Solarix XR) was used to identify intermediates and degradation products; method parameters are described in Table S2 (Supporting Information).

The removal percentage of pharmaceuticals was calculated according to the difference between the initial concentration and the concentration after time t, by the following equation:

$$q_t = \left(\frac{C_0 - C_t}{m} \right) V \tag{10}$$

where C_0 is the initial concentration of PhACs (mg/L), C_t the concentration at time t (mg/L), m the mass of catalyst (mg), and V the volume of solution (L).

Using a nonlinear regression method, the pseudo-first-order model was fitted to experimental data of concentrations processed as a function of time, providing rate constants (k, in min^{-1}) as follows:

$$C_t = C_0 e^{-kt} \tag{11}$$

Arrhenius's equation was used to estimate the activation energy of reactions:

$$k = Ae^{-\frac{E_a}{RT}} \tag{12}$$

where k was the rate constant, R the universal gas constant, T absolute temperature (in Kelvin), A the constant for each reaction, and E_a the activation energy.

The effects of solution pH, temperature, catalyst loading, Oxone® dose, PhACs concentration, scavenger, and water matrix were studied by varying the corresponding parameter. The extent of mineralization was monitored by measuring the total organic content using a TOC analyzer (Shimadzu, TOC-$V_{CPH/N}$). The concentration of PMS was quantified by means of a colorimetric method [71]. Quantification of leached CNTs was obtained from UV–vis measurement at λ_{max} = 800 nm. For reusability tests, the spent-foam was magnetically isolated, washed with deionized water under sonication, and re-used in four consecutive cycles. The reproducibility was verified by replication, blank and control tests; the reported standard deviations in key figures were obtained by triplicate experiments.

The mechanistic study was carried out via detection of reactive species-trapping reagent (DMPO and TEMP, 0.1 M) adducts by EPR equipment (Bruker EMS-plus) as well as solvent isotope effect study. The role of potential reactive oxidizers was investigated using

Table 1
Summary of materials and preparative methods.

| Abbreviation	Description	Synthesis protocol
p-SW	pristine single-walled CNTs	None
pu-SW	purified single-walled CNTs	- 300 °C in air, 30 min
		- 3 M HCl washing, 6 h
F1	Hybrid F1	- p-SW (0.5 g), D-glucose (1 g), ammonium carbonate (1 g), and citric acid (0.7 g)
		- 160 °C for 1 h and 450 °C for 3 h
F5	Hybrid F5	As above, except citric acid (3.5 g)
F1-a	Hybrid F1-a	Annealing F1 at 600 °C (heating rate 3 °C/min, holding time 1 h) in N_2
F5-a	Hybrid F5-a	Annealing F5 at 600 °C (heating rate 3 °C/min, holding time 1 h) in N_2
F1-a^{12h}	Hybrid F1-a^{12h}	Annealing F1 at 600 °C (heating rate 3 °C/min, holding time 12 h) in N_2
N,C/Cel	Reference material	- Cellulose (0.5 g), D-glucose (1 g), ammonium carbonate (1 g), and citric acid (0.7 g)
		- Annealing as F1-a
N,C/AC	Reference material	- Activated carbon (0.5 g), D-glucose (1 g), ammonium carbonate (1 g), and citric acid (0.7 g)
		- Annealing as F1-a
C/SW	Reference material	- p-SW (0.5 g), D-glucose (1 g).
		- Annealing as F1-a
Fe₃O₄	Reference material	See Text S1, Supporting Information.
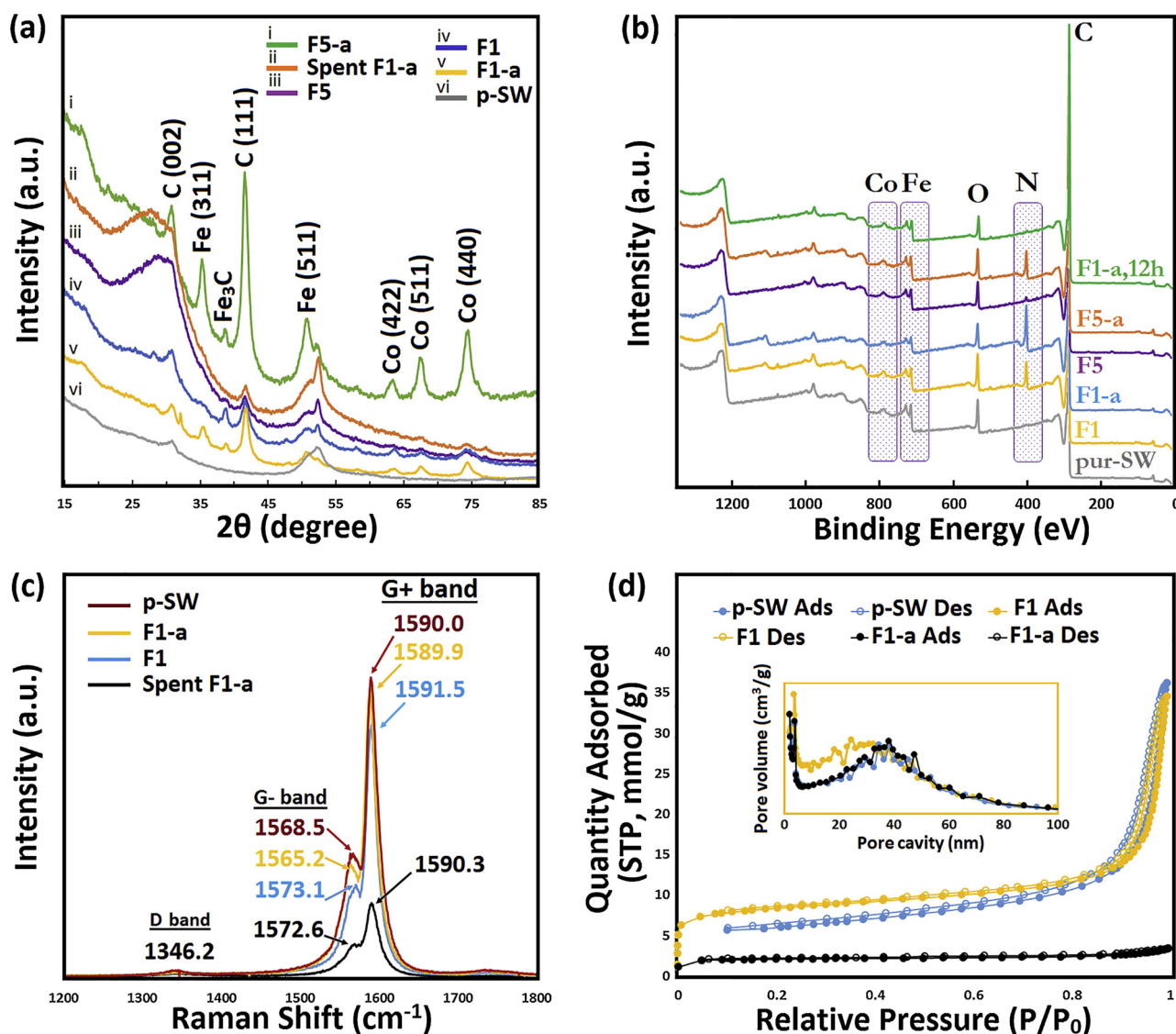
Fig. 1. Structural, surface features and textural porosity of the fabricated materials.

scavenging experiments in methanol (MeOH), *tert*-butanol (TBA), and sodium azide (NaN₃) with or without solvent exchange.

3. Results and discussion

3.1. Characterization of carbofoams

As shown in Fig. S1a-i, the hybrids were assembled out of a spongy skeleton homogeneously covered by biomass-derived carbon. The coating layers glued the tubules maintaining its hierarchical architecture with intertwined bundles and macropores. Residual catalyst particles were observed on and within the nanotubes. The surface of p-SW changed to rough, bumpy and thick (≈ 31 nm) upon calcination (Fig. S1). From TEM images, smooth and thin (≈ 11 nm) tubules were observed after pyrolysis, representing additional stacked shells. An insight into the crystal structure was provided by diffractometer with broad and intense reflections at 29° and 42° for both F1-a and F5-a implying the loading of N, O onto carbon matrix [17–19,37,38]. PXRD peaks of metal species were absent in p-SW, but apparent in the hybrids (Fig. 1a). Carbon reflections appeared to increase upon annealing and sp³-to-sp² conversion. The widened full width at half maximum of the (002) peak in F5, F5-a, and F1-a likely indicates an interruption of amorphous phase [36,42]. The graphitization was reported to improve

PMS disintegration by enabling electron transfer along sp² network and at interfaces of heteroatom-active metal species-carbon [28,42].

Figs. 1b and S2a depict the surface elemental composition and chemical configurations. Three observed distinctive peaks are attributable to C1s, N1s, and O1s. The metal portion mainly consisted of Fe, Co, and Mg and reduced to 2.5 at.% on F1-a (Table S3). Fitting C1s spectra revealed a shoulder (285.4 eV) and a small peak (289.5 eV), partly ascribable to N-sp²-C and N-sp³-C bonds. Remarkably, 11.8 at.% of N was detected on F1-a, showing that the doping occurred close to the nanotube plane where O-containing moieties likely promoted carbon-dopant interactions during slow thermolysis [38,39,41]. Part of N thus could be anchored by metal species allowing the shells to shield the bulk constituents and allocate dopants to active sites. Deconvolution of N1s envelopes reveals characteristic components at 398.0 (42.32%), 399.7 (12.24%) and 401.6 eV (36.82%) of pyridinic, pyrrolic-N and quaternary/graphitic-N, respectively (Fig. 2a), indicating the heteroatom richness in the carbon lattice [39,42]. The (399.7 eV) peaks could embody N-species in coordination with iron and cobalt (Me-N$_x$) [42,43]. A minor shoulder at 403.7 eV (8.61%) links to oxygenated-N and surface adsorbed-N species. The abundancy of N-species was in order: pyridinic/Me-N$_x$ > graphitic > pyrrolic > N-oxide; graphitic-N and pyridinic/Me-N$_x$ contents increased upon annealing. This is an important feature because higher graphitic-N can facilitate
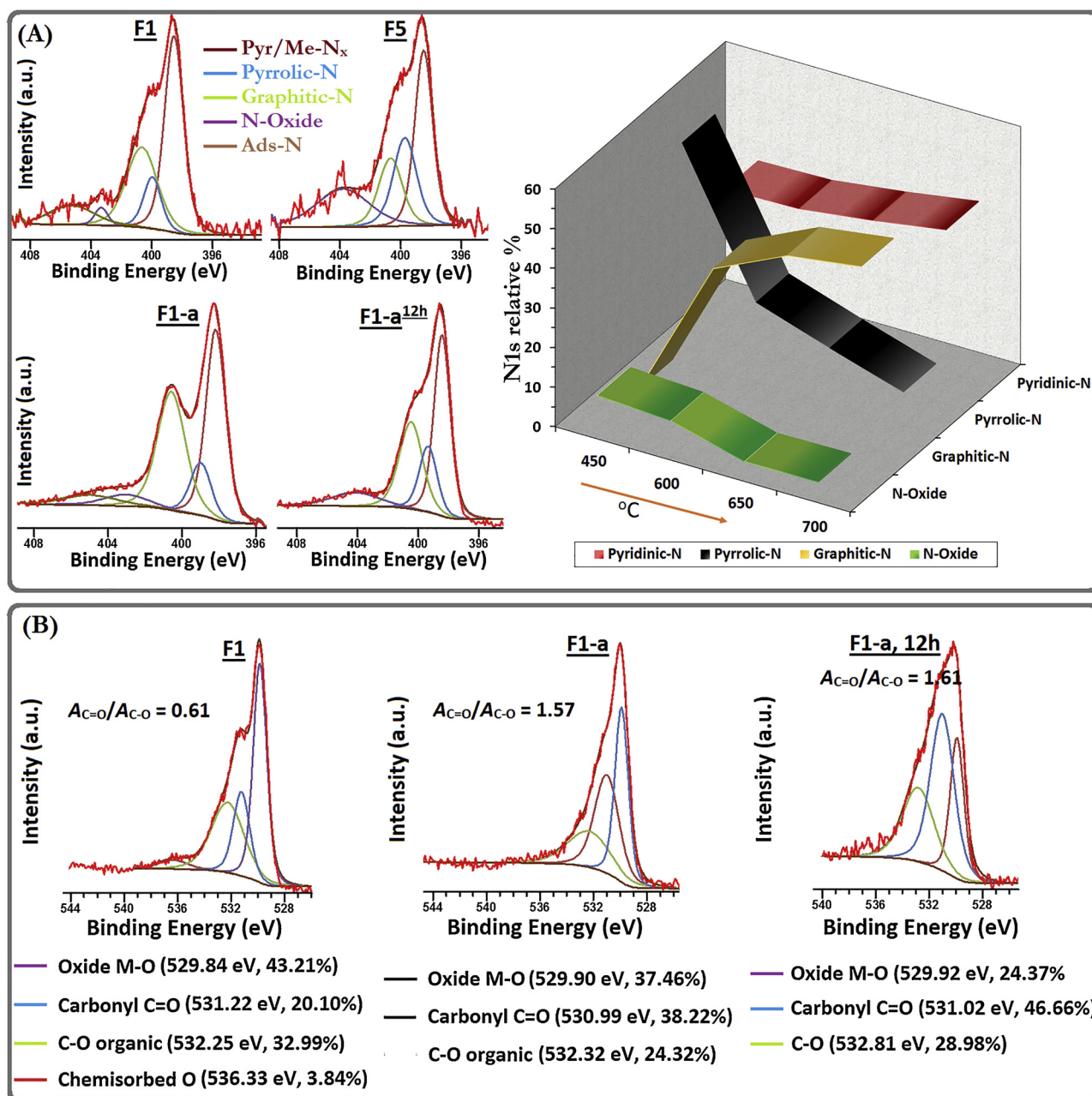
Fig. 2. (A) Deconvolution of high-resolution XPS spectra of N1s region for selected composites and relative composition of surface N-functionalities on F1 at different pyrolysis temperature; (B) The evolution of O-containing groups.

the generation of non-selective radicals [34,64,67], whereas Me-N_x-C interfaces can be promoted to catalytically active sites [38–43,70]. It is well-established that excessive O-containing groups react with N species, forming thermal stable graphitic-N and releasing the defective edges [28,52,53]. Indeed, pyrolysis helped to increase fivefold in graphitic-N content whereas oxygen species increased twice in calcined composites then reduced upon annealing. FTIR analysis supports this with assignable stretching vibrations of C≡N, C=N bonds, and vibration modes of N-heterocyclic rings (Fig. S3). The enriched pyridinic- and graphitic-N fractions have been demonstrated to enhance the catalytic performance of N-doped carbonaceous materials [12,19,28,38,42], which might imply higher reactivity of the annealed foams towards PMS activation. Deconvoluted O1s spectra showed that F1-a contained more carbonyl O than that of F1. A small quantity of C–O/C−OH could be merged with C=O at 531–532 eV but an increased $A_{C=O}/A_{C-O}$ ratio evidenced the conversion of surface-bound O

into more thermally stable carbonyl group (Fig. 2b). The detachment of N species and enrichment of O in spent catalysts (Fig. S4 and Table 2, entry 8, 9) are most probably generated from the oxidation process [67].

The variation in structural disorder and defects were evaluated using Raman spectra where D-band and G-band had intensities referable to the magnitudes of defects and graphitization, respectively. Compared to F1, higher I_G/I_D ratio (≈ 43.5) and broader D-band of F1-a indicated an annealing of defect-rich coatings and structural distortions. Altogether with XRD and XPS results, the high degree of graphitization of F1-a indicated the successful incorporation of heteroatoms into the ordered graphite lattice.

Introducing heteroatoms and assembling graphitic-rich layers benefited the permanent porosity, distinctively characterized with type-IV isotherms for a mesoporous structure (Fig. 1d). In comparison to p-SW, the hybrids had notably improved porosity (Table 2). Pyrolysis-

Table 2
Porosity and XPS characterization of the CNTs-based hybrids.

entry	sample	Textural porosity				Relative composition[e]			
		S_{BET}[a]	V_t[b]	V_m[c]	PSD[d]	C	O	N	N/C
1	**p-SW**	417	1.20	0.072	2.0; 3.5; 38.5	97.40	2.60	n.d.	
2	**pu-SW**	431	1.37	0.076	2.0; 3.8; 38.1	95.85	4.15	n.d.	
3	**F1**	690	1.25	0.177	2.0; 2.6; 3.8; 38.1	91.97	5.58	2.45	0.03
4	**F5**	583	1.16	0.190	2.0; 2.5; 3.8; 38.5	92.78	5.70	1.52	0.02
5	**F1-a**[12h]	579	1.12	0.078	1.3; 2.0; 2.6; 3.4; 34.4	93.84	5.21	0.94	0.01
6	**F1-a**	239	1.18	0.062	1.3; 2.0; 2.5; 3.4; 38.0	83.77	4.45	11.78	0.14
7	**F5-a**	215	1.120	0.060	1.3; 2.0; 2.4; 3.4; 38.7	86.67	4.61	8.72	0.11
8	**5th run F1-a**	185	1.159	0.049	2.0; 3.8; 38.0	86.54	5.53	7.93	0.09
9	**5th run F5-a**	155	1.120	0.040	2.02; 3.8; 38.3	86.88	8.15	4.97	0.06

n.d.: not detected.
[a] Specific surface area (m^2/g).
[b] total pore volume (cm^3/g).
[c] t-plot micropore volume (cm^3/g).
[d] Pore size distribution (nm).
[e] Atomic % estimated by XPS analysis excluding metal species.

induced layers stacking and moieties elimination reverted samples to lower microporosity and moderate S_{BET}. The annealed foams have a 3-time-smaller S_{BET} and micropore volume than the F1 and F5 but similar total volumes is maintained. Broad pore size profiles with maxima centers at 2.02 nm followed by mesopore domains and expansive macropores might favor pore wetting and diffusion in the aqueous phase. Graphitization promoted the stacking of layers to ≈1.3 nm and reduced mesopore range while excessive citric acid yielded greater O content (Table 2, entry 4, 7).

Fig. S6 illustrates the thermal profiles of samples, registering a weight-loss of approximately 80% (F1 and F1-a) to 88% (F5 and F5-a) around 500 °C. The p-SW is stable below 600 °C with complete weight loss was observed at around 750 °C. The DTG curves recorded on calcined hybrids contain two stages (582 and 595 °C in F1; 495 and 595 °C in F5) ascribable to the oxidation of amorphous and graphitic carbon, respectively. F1-a, however, exhibited a single peak at 485 °C while F5-a had a distinct drop at 510 °C and a small shoulder at 680 °C. This high thermal stability might enable the application of thermal processes to the exhausted catalysts to desorb bound intermediates and regenerate catalytic power. Previous studies showed that heteroatoms of the desired binding states could be facilely tweaked by manipulating the doping dose at high temperature (600–1000 °C) [18,19,34,41]. Here, lengthening pyrolysis faced a drop of N-content in F1-a[12h], speculating that 1 h annealing at 600 °C was reasonable to balance doping and graphitization. The roles of the modulated textural properties and chemical compositions in the catalytic oxidation of PhACs will be concretely discussed below.

3.2. Adsorption and degradation performance

First, the general capability of the prepared materials in water remediation was examined in the adsorptive and PMS-based oxidative removal of phenol. Next, comparative studies were investigated for ATN using various materials, followed by a comprehensive comparison of all target PhACs using selected carbofoams.

As shown in Fig. S7, F5 provided the highest phenol uptake (56% in 80 min) while the pyrolyzed foams removed 20% of phenol (C_0 = 10 mg/L) via adsorption. Having PMS in the solution, the catalyzed oxidation processes achieved complete phenol removal in 1 h. The efficiencies in phenol abatement encouraged targeting model PhACs. Figs. 3a-b show that PMS itself brought no concentration reduction, implying negligible self-activated oxidation. Adsorptive removal by foams was superior to the oxidation capacity of Fe_3O_4@PMS system. The catalytic efficacies towards degradation were increased in the following order: PMS (no catalyst), Fe_3O_4, N,C/Cel, N,C/AC, F5-a,

F1-a, F5, and F1. The pu-SW, p-SW and C/SW samples were clearly less potent than the carbofoams, likely due to their intact graphitic structure barely contains active species.

Specifically, ATN decay by F5-a was slower than that by F1-a while F1 and F5 depicted a similar trend (Fig. 3a). A complete disappearance of ATN was attained in 3 h over F1-a but only 90 min over F1. Among CNT-based activators, the pu-SW displayed the poorest catalytic power. The p-SW showed rapid dynamics in the first 30 min but 41% ATN removal required 3 h. Prolonged pyrolysis did not endow better catalysis as 3 h treatment degraded only 65% of the target, compared with a complete decay in 2 h over F1 or F1-a. This finding attributed the improved efficiency to PMS-activation enhanced by the developed active interfaces. The F1@PMS system achieved the greatest ATN degradation compared to F1-a@PMS and F1-a[12h]@PMS, denoting the significance of binding moieties in the adsorption and catalysis processes. Doping electronegative N atoms into carbon lattice causes adjacent C to be positively charged, promoting the formation of reactive outer-sphere PMS complexes via electrostatic interaction [12–14,21–24]. Previous studies suggested that these surface-complexed oxone could act as an electron acceptor and direct non-radical activation pathway [15,16,18,19]. Thus, F1-a that contains sufficient graphitic and pyridinic-N would be an effective mediator towards non-radical route, compared to the other derivatives. Furthermore, F1-a and F5-a that hold more surficial carbonyl would effectively accelerate the self-decomposition of PMS into singlet oxygen [20,21,25,28]. Active metal species have been loaded to carbonaceous materials to induce reductive conversion of PMS into sulfate radicals, thus boosting up radical-induced oxidation [20,26,27]. It is noteworthy that upon annealing, the surficial Co/Fe species was maintained but being transformed into surface-bound Me-N_x-C interfaces thus promoting the non-radical PMS activation. However, the annealed graphitic surface with lower microporosity would slowed down the wettability and binding capacity, respectively, compromising the kinetics. A good correlation between the removal efficiency of PhACs and the all-in-one catalyst properties was not clearly observed, probably due to multivariate contributing factors counterbalanced the potential synergized effects [19,28]. Although the catalytic performance varied with target substrate, the synergetic effects of active functionalities, defects, sp^2 network and accessible storing cavities remained pivotal for the observed PhAC removal.

The decomposition rate depends on the crystallinity, morphology, and porosity of the catalyst. Molecular descriptors of targets also condition adsorptive affinity and oxidative reactivity. Fig. 3c-f illustrate the annealed foams carrying much less ATN and IOP than the other hybrids. Particularly, sorption equilibria were attained in 30, 120, 120,
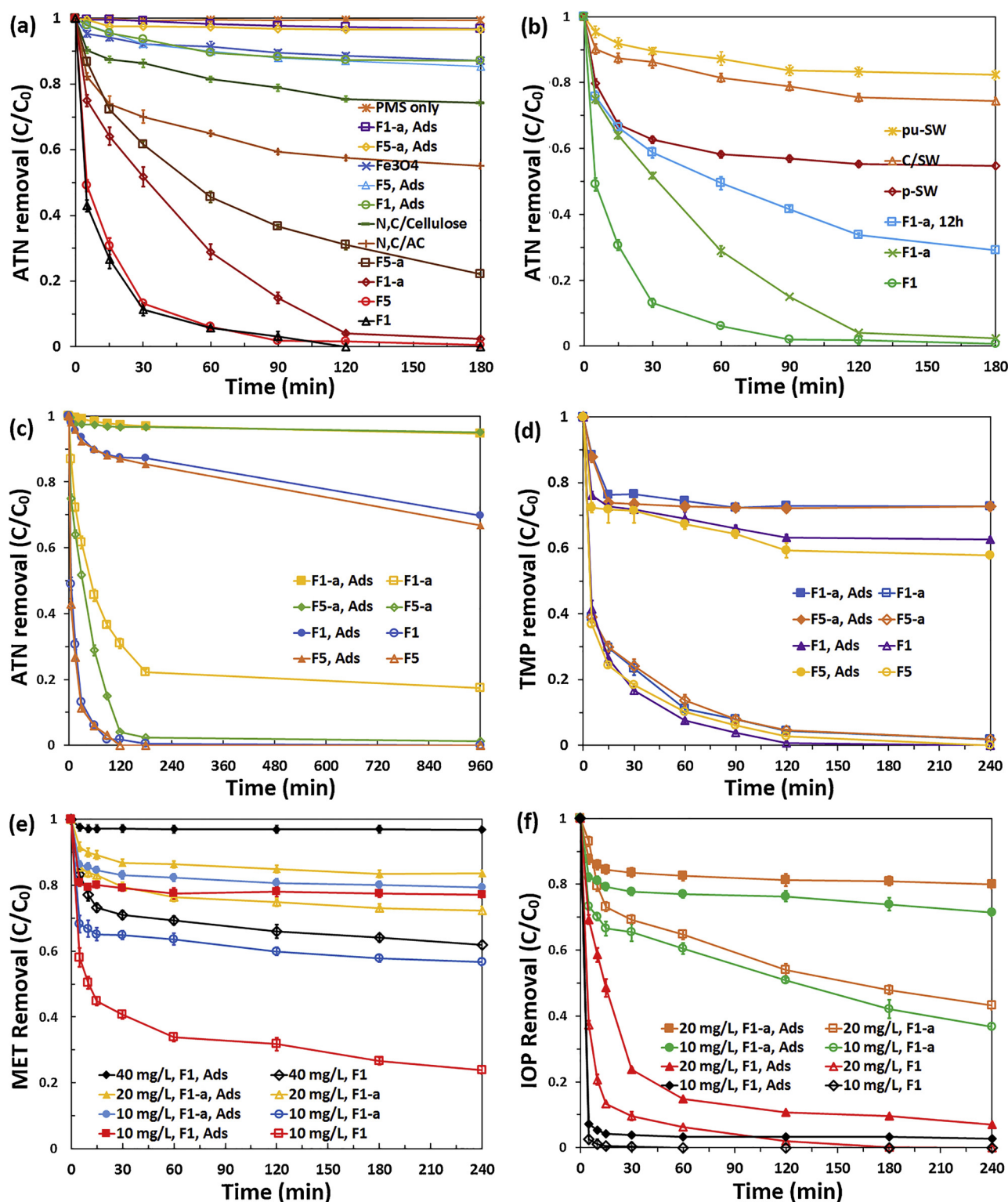
Fig. 3. Performance of different materials in the removal of (a, b) ATN and c–f) PhACs in various scenarios ($[PhACs]_0 = 10 \, mg/L$; native pH; [catalyst] = 0.1 g/L; with or without $[PMS]_0 = 1 \, g/L$; $25 \pm 2 \, °C$).

and 960 min for IOP, MET, TMP and ATN, respectively. F1 had reluctances to ATN and MET ($\approx 22\%$ removal) but offered 40 and 98% TMP and IOP disappearance in 2 h, respectively. The equilibrium concentrations of MET (7.8 mg/L) and IOP (0.5 mg/L) correspond to 0.13 molecules/nm^2 coverage. The capability of F1 to house voluminous IOP molecules, despite a high initial concentration of 20 mg/L, can be attributed to its moiety richness and hierarchical porosity. Having

threefold less V_m, the annealed foams underwent similar tendency but were less potent in sequestering PhACs. The most detrimental effect observed in IOP uptake by F1-a (≈ 0.028 molecules/nm^2) is ascribed to its distinct molecular dimensions and a restricted microporous accessibility [70]. High catalytic activities of F1 and F5 towards ATN and IOP likely originated from the hydrophilic surfaces of higher S_{BET}, which facilitated direct conversion of oxone and target substrates on foam
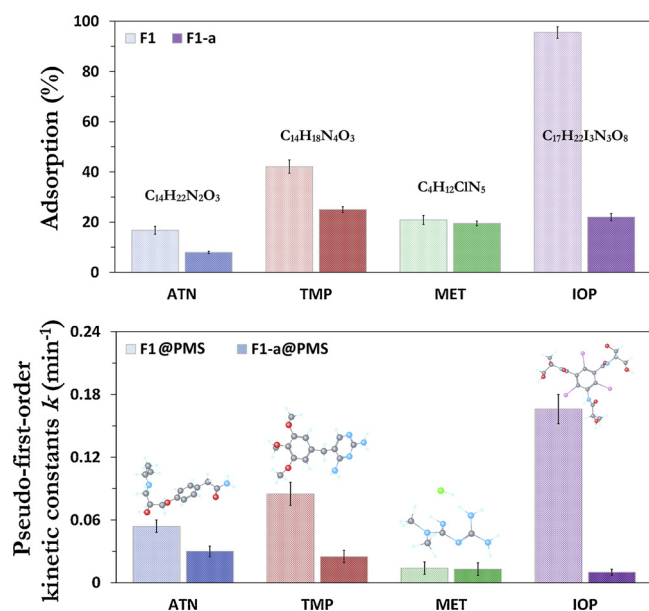
Fig. 4. Relative adsorption and reaction rate constants in F1@PMS and F1-a@ PMS systems. Conditions: $[PhACs]_0 = 10$ mg/L; native pH; [catalyst] = 0.1 g/L; with or without $[PMS]_0 = 1$ g/L; 25 ± 2 °C.

surfaces. In both cases, the hierarchical porous architecture could shorten transport to binding sites for accelerated oxidation processes [19,22].

A 60-min exposure to PMS provoked 92, 97, 68, 99% and 71, 90, 45, 40% conversion of ATN, TMP, MET, IOP over F1 and F1-a, respectively. F1 retained a 96% initial amount of IOP within 5 min and remained relatively equilibrated before adding PMS completely degraded the residues in 15 min. Apart from the adsorptive fraction, the oxidative removal of ATN accounts for 78, 89, 90, and 98% by F5-a, F5, F1, and F1-a, respectively. The recalcitrant level to degradation was in decreasing order: MET, ATN, TMP, IOP (Fig. 4). Metformin was the most refractory contaminant, although the removal rates were improved comparing to the UV$_{254}$/H$_2$O$_2$/Fe(II) system [51]. The slower kinetics over F1-a and F5-a can be ascribed to their lower porosity, thus hosting capacities towards PhACs. It is not excluded that the selective nature of singlet oxygen, which the carbonyl-enriched annealed foams have higher propensity for [18,19,28,40], compromised its oxidative capacity (e.g. towards MET). The overall performances within the same timeframes (2 h) showed minor differences, presumably attributed to the modulated catalytically active moieties. Previous studies suggested the electron transfer from organic substrates to surface-bound oxone via carbon network [10,39,68]. The non-radical was also deduced when Me-N$_x$ species were in contact with the carbon lattice, changing the chemical configurations, electron and charge densities of the carbon atoms [38,73,76]. Although the metallic contents relatively unchanged, the iron and cobalt species encapsulated under graphitized shells might facilitate the catalysis by tuning the electron densities in the surficial carbons [39,40,70]. Therefore, F1 and F5 foams offered better uptakes but minor discrepancies in oxidative capacity comparing to F1-a and F5-a, indicating the significance of both structured porosity and catalytically active Me-N$_x$-C sites.

The catalytic performance in terms of rate constants also depends on functionalized alien atoms. The accommodation of ketonic groups within the hybridized carbon can facilitate electron flows to oxone, leading to enhanced evolution of radicals. Recent studies elucidated that C=O activates PMS similarly to graphitic N-enriched CNTs and high-temperature carbonization worsens catalytic power [27,36]. Here, higher-temperature annealing endowed limited kinetics improvement (Table S4), whereas prolonged annealing lead to a lower doping level but increased rate constants, trackable to a highest carbonyl content as

estimated by XPS. Both graphitic-N and carbonyl moieties thus synergistically contributed in disintegrating PMS for the oxidation process. However, not only the modulated properties of carbofoams but also the operating conditions substantially affect persulfate activation routes and degradation performance.

3.3. Effects of operating parameters

3.3.1. Thermal agitation

Environmental conditions such as temperature, solution pH and water background composition have an important effect on degrading pollutants. Oxidations of organic contaminants mediated by PMS are often temperature-dependent, partly because of its thermal-promoted activation [47–56]. Elevated temperature may also stimulate non-target reactions, making it an important control parameter in complete PhACs removal. Showing poorer uptake capacities, F1-a was selected for temperature-dependence tests. Results showed that thermal agitation positively improved degradation kinetics; 2 h were sufficient to attain 99% TMP disappearance at 308 K and complete ATN decay was attained in 180 min at 328 K (Figs. 5a and S8). The E_a values for IOP, ATN, TMP, and MET in F1-a@PMS system were estimated to be ≈15.8, 19.0, 28.6, and 57.9 kJ/mol, respectively. The removal of electron-rich MET could be elevated at higher temperatures, which facilitate electron transfer in the radical generation process [17,38,67]. In contrast, sharing the need of energy input to concurrent reactions between oxidizers and high-molecular weight intermediates hindered fast IOP conversion [53–55].

3.3.2. Catalyst and Oxone® dose

The effects of catalyst and oxidant loading on degradation are shown in Figs. 5b,c and S9. The reaction rate rapidly increased with catalyst or oxidant loading, ascribable to the availability of active species. Despite the kinetics improvement at higher Oxone® dose, the increment was beneficial up to 0.5 g/L; above this dose, degradation dynamics reached a plateau. As depicted in Fig. S9, increasing oxidant promoted ATN elimination from ATN + TMP binary mixture. A tap water matrix required 2 g/L Oxone® for 27 and 65% removal of MET and IOP, respectively. In contrast to a gradual temporal decay of MET, IOP underwent a tailing kinetic pattern, revealing a competitive consumption of reactive oxidant and inhibitory effect by background molecules [58]. It is not excluded that degraded products and matrix constituents pre-occupied binding and catalytic active sites and slowed down the target reactions. This observation signifies that the PMS dose is the key limiting factor for practical complete elimination of PhACs. However, low dose was more preferred to avoid self-decomposition and the risk of sulfate anion pollution in the effluent [6,17,54].

3.3.3. PhACs initial concentration

Figs. 5d and S10 presented the influence of pollutant loading. Obviously, concentrated solutions marked lower kinetics. These tendencies closely reflected the nature of PhACs, surface charge and functionalities. As discussed earlier, adsorption affinity decreased in the order: IOP, TMP, ATN, to MET and was favored more on air-calcined hybrids than their N$_2$-annealed counterparts. Fig. S11 shows increased r_0 values of F1-a foam for ATN, TMP, and IOP but not MET, the cationic molecules with one hydrogen-bond acceptor. Owning seven H-bonding sites and smaller topological polar surface area, ATN experienced less fall in r_0 comparing to the voluminous IOP. Thus, the structures of PhACs induced specific interactions with the carbofoams, varying the degradation efficiencies especially for highly concentrated substrates and process controls are needed to reach a desired reduction of target compound and concentration.

3.3.4. Initial pH

Solution pH is an important factor in determining the speciation of PhACs, PMS [5,8] and catalyst functionalities [66–70]. It has been
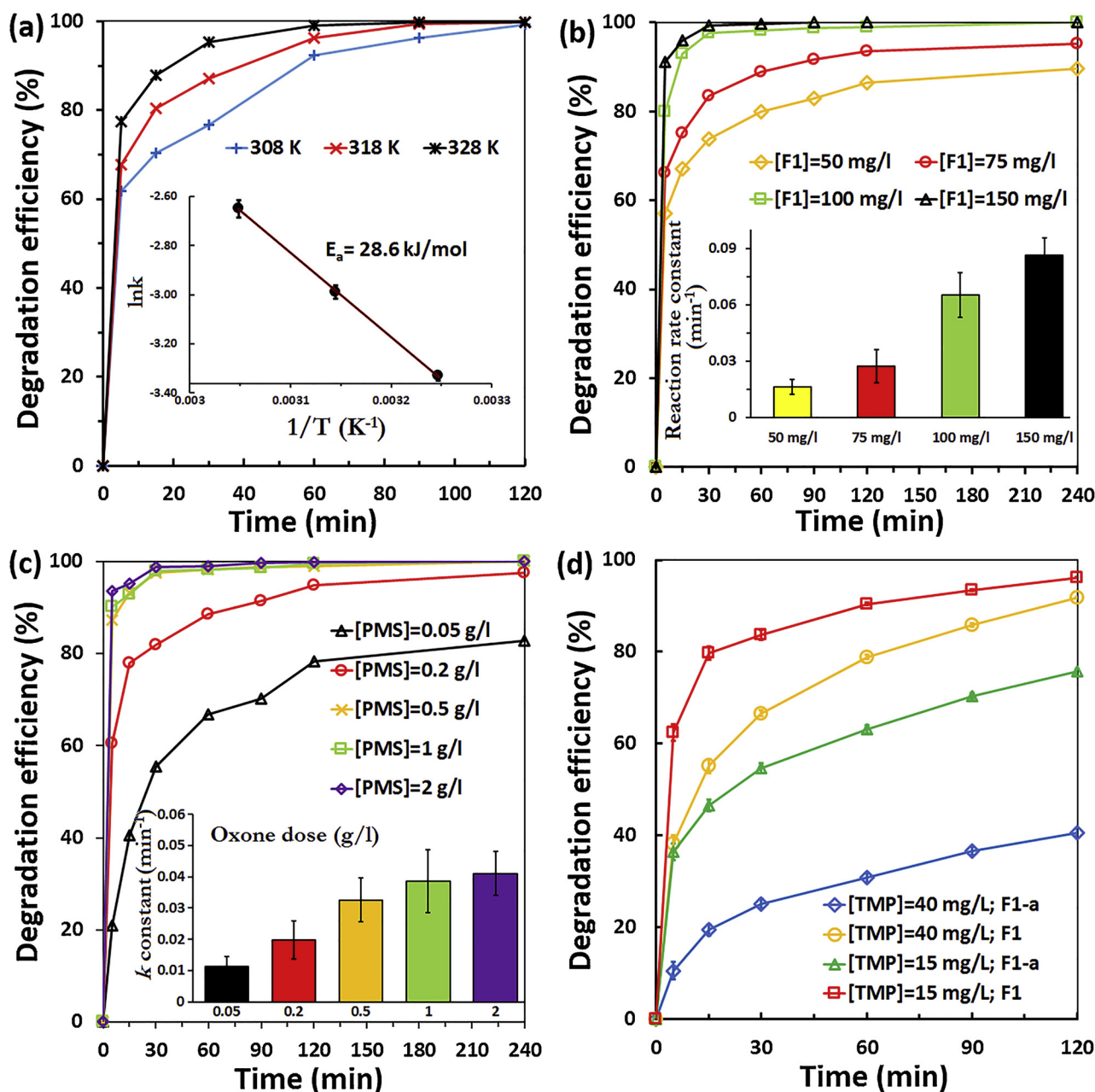
Fig. 5. Influence of (a) temperature dependence, (b) catalyst loading, (c) oxidant dose and (d) pollutant loading on TMP removal. Conditions: [F1-a] = 0.05 g/L (a); $[PMS]_0$ = 2 g/L (b); [F1] = 0.1 g/L (c); [catalyst] = 0.05 g/L; $[PMS]_0$ = 2 g/L (d); 25 ± 2 °C.

reported that $SO_4^{•-}$ predominates at pH < 7, both $•OH$ and $SO_4^{•-}$ present at pH 9; and $•OH$ is the principal radical at pH 12 [8,9]. Fig. 6 shows that pH_0 slightly affected the initial reactivity and rate constant. Generally, the initial r_0 over F1-a increased with initial pH higher than 9 but the opposite was observed for F1 whereas k values were higher in F1@PMS than those catalyzed by F1-a. Alkalinity enabled negatively charged moieties to repulse dianionic SO_5^{2-} and PhACs, especially the deprotonated ATN and TMP, leading to a suppressive interaction and less conversion at interfaces. Singlet oxygen and superoxide radical were less interfered by water background and stimulated a stronger attack on electron-rich targets, thus regulating reaction dynamics at high alkalinity [68,67–70,75]. At pH 11, MET still remained monoprotonated [74] and IOP did not dissociate, resulting in trivial activity depletion. Because PMS hydrolysis quickly acidified solutions (Table S5), such positive factors partly offset the inhibition while electrostatic repulsion, radical abundance, and PhACs speciation governed the

overall transformations. Conclusively, the initial pH_0 had insignificant impact to the overall removal rates.

3.3.5. Water matrix and organic matter

Water background plays an important role in the efficient oxidative degradation of PhACs [46–55,75,76]. Catalyst deactivation and suppression of oxidizers could restrain conversion processes [55,67]. Thus, the impacts of ubiquitous inorganic anions, natural organic matter, and competitive compounds were examined. The rate constants of reactions interfering by bicarbonate and chloride ions are presented in Table 3. Generally, the predominance of these anions hampered catalysis, possibly under shielding effect and transformation of oxidants into less reactive species [53,77]. The inhibitory effects of bicarbonate were minor at 1 mM but relatively severe at higher concentrations. In contrast, at 10 mM Cl^- the rate constants slightly increased. Previous studies have demonstrated that chloride can be activated by PMS via
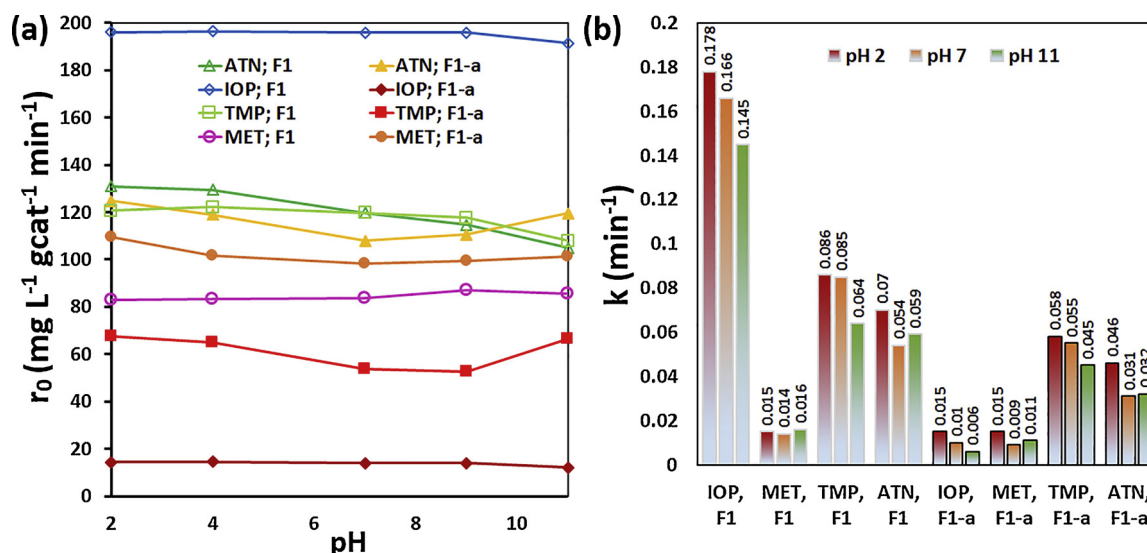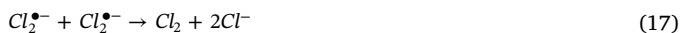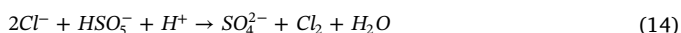
Fig. 6. Initial pH_0 effect on the initial activity (a) and apparent reaction rate constants (b) of carbofoam@PMS catalysis. Conditions: $[PhACs]_0 = 10\,mg/L$, unbuffered; $[catalyst] = 0.1\,g/L$; $[PMS]_0 = 1\,g/L$; $25 \pm 2\,°C$.

both non-radical pathways (Eqs. (13) and (14)) and sulfate radical-mediated pathways (Eqs. (15)–(19)) [50,80,81].

$$Cl^- + HSO_5^- \rightarrow SO_4^{2-} + HOCl \quad (13)$$

$$2Cl^- + HSO_5^- + H^+ \rightarrow SO_4^{2-} + Cl_2 + H_2O \quad (14)$$

$$SO_4^{\bullet-} + Cl^- \rightarrow SO_4^{2-} + Cl^\bullet \quad (15)$$

$$Cl^\bullet + Cl^- \leftrightarrow Cl_2^{\bullet-} \quad (16)$$

$$Cl_2^{\bullet-} + Cl_2^{\bullet-} \rightarrow Cl_2 + 2Cl^- \quad (17)$$

$$Cl_2^{\bullet-} + Cl^\bullet \rightarrow Cl_2 + Cl^- \quad (18)$$

$$Cl_2 + H_2O \rightarrow H^+ + HOCl + Cl^- \quad (19)$$

Therefore, the generation of reactive halogen and oxychlorine species would alter the degradative route, oxidation efficiency and product distribution. Attempts to correlate chloride concentration with degradation rate have been explored in previous studies [80–85]. The possible generation of sulfate radical from PMS self-decomposition at room temperature may complicate distinguishing the contribution of non-radical and radical pathway [81]. Yuan et al. reported the various effects of chloride (0–500 mM NaCl) on Co^{2+} mediated-dye bleaching with reaction rates increased exponentially with chloride and PMS content [82]. Yang et al. observed that the amount of adsorbable organic chloride sharply increase in the degradation of Methylene Blue over PMS/Cl^- system ($[PMS]_0 = 1\,mM$) with the Cl^- concentration increasing from 0 to 300 mM [83]. Rivas et al. demonstrated that chloride (6×10^{-5}-$22.5 \times 10^{-4}\,M$) slightly accelerate the decomposition of PMS (0.05-0.2 M) for tritosulfuron degradation [84]. Reently, Hou et al. reported that a very small amount of HOCl/OCl$^-$ (1.86 μM) could be generated by reacting chloride (20 μM) with ten-fold molar excess PMS [85]. Indeed, different conversion patterns of chloride

(0.2–1000 mM NaCl) by PMS (2 mM) were observed (Fig. S12). The generated reactive chlorine species can react with PhACs contributing to their accumulated depletion, especially electron-rich PhAC species, which are greatly vulnerable to chlorination and oxychlorination [68,72,78]. Probably, Cl^- interaction with electron-rich intermediates enables by-product transformations via H-abstraction and electron oxidation [79,80]. Strong ionic strengths ($> 50\,mM$) may also appreciably shifted the mass transport flow and surface interactions on the hydrophobic carbofoam, suppressing the catalysis. Halogenated by-products, which are often more recalcitrant than the parent compounds [86], may have competed with the target substrate for the reactive oxidant, leading to the decreased reaction rates under monitoring.

Fig. 7 shows the impact of two scavengers naturally abundant in organic matter: tannic (TA) and gallic acid (GA). Comparing to TA, the smaller GA molecules would anchor better onto catalyst cavities via strong π-π stacking and outcompete PhACs for binding sites. During oxidation process, these phenolic compounds and their mineralized transformation products also strive for the reactive oxidants. Indeed, removal rates were highly inhibited by GA, followed by TA. Both acids marginally decelerated TMP oxidation, while the distinct structure of MET made it hardly strive in the competition. Under similar conditions, MET removal was suppressed five times, whereas TMP persisted more than 80% degradable. A 24 h monitoring after a secondary dose observed 99, 92, 80 and 35% TMP, IOP, ATN, and MET removed, respectively. Nevertheless, high loadings of phenolic acids considerably impaired PhACs degradations. The maintenance of process parameters or pre-treatment for non-targeting and scavenging compounds should be considered in order to meet the desired water quality [52,58].

Having equivalent $logK_{ow}$ values, MET and IOP can strongly compete each other in simultaneous remediation. The target oxidizing attacks are further restricted where water constituents (peptides, cations, anions) are available as impending scavengers. The simultaneous

Table 3
Effects of inorganic anions on degradation rate constants of TMP and IOP.

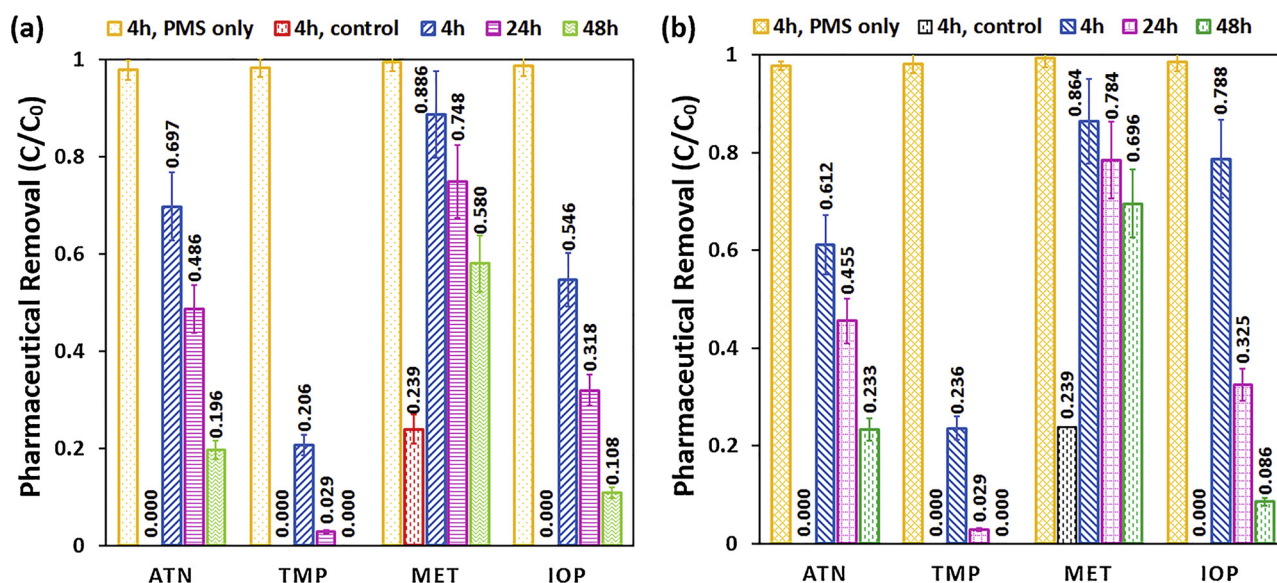| PhACs	Catalysts	HCO$_3^-$				Cl$^-$				Anions (mM)
		0	1	5	10	0	5	10	50	
TMP	F1	0.048	0.046	0.029	0.015	0.048	0.040	0.053	0.009	**Rate constants**
	F1-a	0.033	0.033	0.021	0.018	0.033	0.025	0.046	0.010	**(min^{-1})**
IOP	F1	0.177	0.169	0.085	0.030	0.177	0.182	0.190	0.095	
	F1-a	0.016	0.015	0.015	0.009	0.016	0.023	0.028	0.009	

Fig. 7. Inhibitory effects of TA (a) and GA (b) on PhACs removal by F1@PMS. Conditions: $[PhAC]_0$ = 20 mg/L, native pH, unbuffered; $[TA]_0$ = $[GA]_0$ = 10 mg/L; $[F1]$ = 0.1 g/L; $[PMS]_0$ = 1 g/L; 25 ± 2 °C.

degradation of MET and IOP in deionized water (MW), tap water (TW), and synthetic wastewater (SW) showed large variances from the single-component solution (Fig. S13). In MW (ideal condition), continuous flows of species on the catalyst surface led to steady catalysis [79]. This was not achievable in SW where 55% IOP disappeared in 5 min but similar efficiency for MET needed 4 h. IOP perhaps pre-occupied binding sites and blocked pores, causing an abrupt cessation of initial activity towards MET. The accumulated conversion of MET over F1-a was 35% in 4 h, compared to 45% attained in the single-target solution, which indicates its recalcitrance. Although it is difficult to correlate molecular descriptors with degradation rates, the high activation energy of MET could partly explain the observations. Nonetheless, kinetics were still prompt at the beginning of reaction before catalytic interactions were impacted, forming tailing curves. For IOP, SW and TW matrices demonstrated no substantial depletion. TW slightly favored MET removal, probably by different complexing effect with background metallic cations. Chloride (0.15 mM) in SW could accelerate PMS decomposition to form hypochlorite, free chlorine and relatively less reactive $Cl^{\bullet}$ and $Cl_2^{\bullet-}$, leading to reduced efficiency [67–69]. Slight discrepancies amongst matrix effects are partly due to the better oxidation of chloride by $SO_4^{\bullet-}$ than $^{\bullet}OH$ [17,68]. Although the least negative effect was observed for IOP in the binary-mixture, sufficient Oxone® doses were critical to reach a complete degradation.

Identifying reactive species and their power in destruction pathways can be supported by scavenging tests, which also reflects the influence of non-targeting substrates to the speciation of free and surface-bound oxidants. As illustrated in Fig. 8a,b, both radical shield alcohols induced strong interference to the removal of TMP; the rate constant reduced from 0.033 to 0.0008 (min^{-1}) with increasing proportion of alcohols (0 to 95 v/v %). In organic solvents, PhACs likely to linger away from catalytic surfaces resulted in a decelerated degradative interaction. The presence of excessive azide (3–10 mM) inhibited ∼25% degradation efficiency of TMP (Fig. 8c). These results indicated the significance of water background on the effective PMS-mediated carbocatalysis.

3.4. Principle reactive oxidizers and activation mechanism

Singlet oxygen, hydroxyl and sulfate radicals have been identified as reactive species formed in PMS decomposition on carbocatalysis [6–28,52–55,66,69–73]. Here, EPR spectra performed on different catalytic systems showed evidences of all the free radicals. The

generated oxidizers were trapped by DMPO and TEMP distinguishing their catalytic powers via hyperfine splitting constants and peak intensities of DMPO-OH, DMPO-SO$_4^-$ and TEMP-$^1O_2$ adducts. Based on the intensity of the DMPO-X adduct, F1 and F1-a appear to be superior than Fe$_3O_4$ in activating oxone. When ATN and TMP were added, the signals of DMPO-X were weakened, suggesting the competitive consumption of generated oxidants by the substrates [28,39,68]. The observation of DMPO-OH and DMPO-SO$_4^-$ peaks after 15 min reaction in different water matrices (Fig. 9b) revealed the existence of hydroxyl and sulfate radicals. It has been reported that graphitic-N, ketonic-O and Me-N$_x$-C sites at defective edges can lower surface energy, bridging electron flows and charge transfer, collaboratively leading to the enhanced evolution of reactive species [28,70]. Highly graphitic carbonaceous surfaces promote the non-radical activation of PMS via mediated-electron transfer [66–70], whereas Me-N$_x$-C interfaces also activate PMS decomposition into highly active $^1O_2$ [18–21,76]. The hypothesized singlet oxygenation was supported with the identification of a triplet pattern of equal intensity characteristic of TEMP-$^1O_2$ adducts (Fig. 9c) [28,40,41,68]. Signal intensity was boosted in the catalyzed systems and wave amplitude decreased as $^1O_2$ may interact with PhACs. Although a quantitative evaluation of individual species remains challenging [6,17,68], F1-a appears to be stronger activator compared to F1 and F5 and it is reasonable to infer that both graphitic-N, carbonyl groups and Me-N$_x$-C sites collaboratively promoted the singlet oxygenation. No peaks were detected for oxone alone, excluding $^1O_2$ formation via PMS self-decomposition. Finally, the reduction of signal intensity in PhACs mixture prepared in synthetic wastewater indicated a rapid consumption of $^1O_2$ by matrix constituents.

To verify the magnitude of quenching effects alcohols and azide caused on the oxidative degradation of PhACs and the role of individual oxidant in the process, classical quenching tests were conducted using TMP as substrate. *Tert*-butanol could selectively quench $^{\bullet}OH$ faster than sulfate $SO_4^{\bullet-}$ ($k_{\bullet OH}^{TBA}$ = 3.8–7.6 × 10^8 M^{-1} s^{-1}, $k_{SO_4^-}^{TBA}$ = 4.0–9.1 × 10^5 M^{-1} s^{-1}, respectively), MeOH was hypothesized to quench both species ($k_{\bullet OH}^{MeOH}$ = 1.2–2.8 × 10^9 M^{-1} s^{-1}, $k_{SO_4^{\bullet}}^{MeOH}$ = 1.6–7.7 × 10^7 M^{-1} s^{-1}, respectively), whereas NaN$_3$ was chosen to corroborate the existence of $^1O_2$ [28,54,68,72]. In Fig. 8, the scavenging effect was enhanced by increasing the probe level, inferring that both radicals and $^1O_2$ were contributing oxidants. The rate constants of reactions under quenching indicated that $^{\bullet}OH$ and $SO_4^{\bullet-}$ radicals exhibited major contribution in TMP oxidation. At 50% v/v solution (corresponding $[TBA]_0$ and

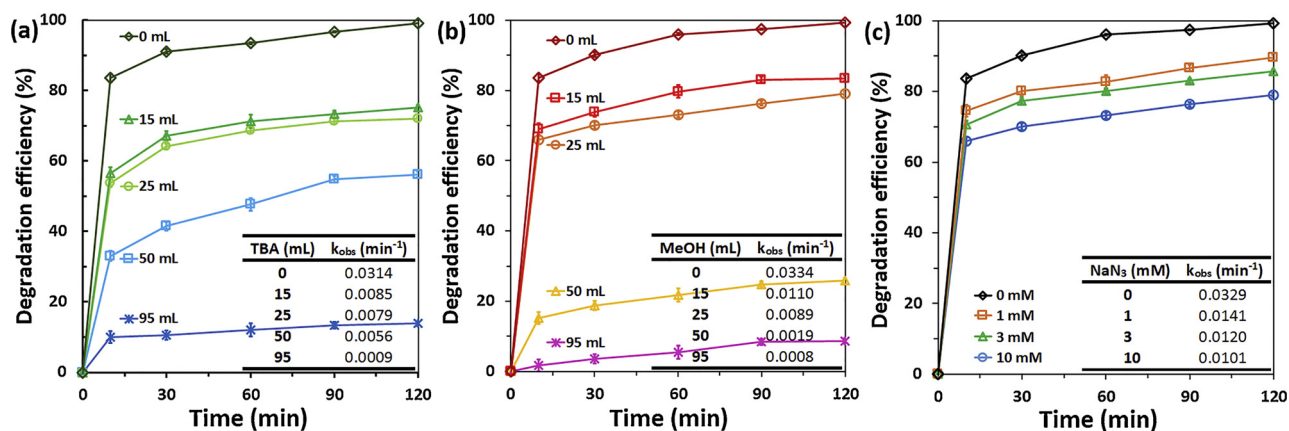**Fig. 8.** Reaction-inhibiting effect of TBA (a), MeOH (b), and NaN$_3$ (c) on TMP degradation in F1-a@PMS. Conditions: [PhACs]$_0$ = 10 mg/L, native pH, unbuffered; [F1-a] = 0.1 g/L; [PMS]$_0$ = 1 g/L; 25 ± 2 °C.

[MeOH]$_0$ ~5.27 and ~12.36 M, respectively), the quenching effects of TBA and MeOH suggested the competitive contribution of the two radicals. The reaction rates of TBA quenching remained higher than that in MeOH (0.0056 vs. 0.0019 min^{-1}, respectively), indicating methanol appears to be more effective for retarding TMP degradation. Regardless the slow hydrolysis of sulfate radical anion at neutral pH, only alcohols in greatly excess (95% v/v, equivalent [TBA]$_0$/[PMS]$_0$ and [MeOH]$_0$/[PMS] was ~3080 and 6800 times, respectively) completely eliminate the oxidative processes, even though TBA barely reacts with SO$_4^{\bullet-}$. The

F1-a and F5-a mediators with probably lower affinities towards water could avoid a complete scavenging the alcohols might have on radicals. The carbofoams would produce surface-bound SO$_4^{\bullet-}$ similar to the pristine and metal-encapsulated nanotubes [14,16,20,26] whereas their 3D hierarchical structure with a superabundance of intrinsic active sites (e.g. defective edges, vacancies, dangling bonds) would enhance the interfacial interactions. The observed behaviors may suggested, beside the electron transfer-based route commonly observed for graphitic carbocatalysts [19,28,41,66,68], here SO$_4^{\bullet-}$-mediated oxidation likely

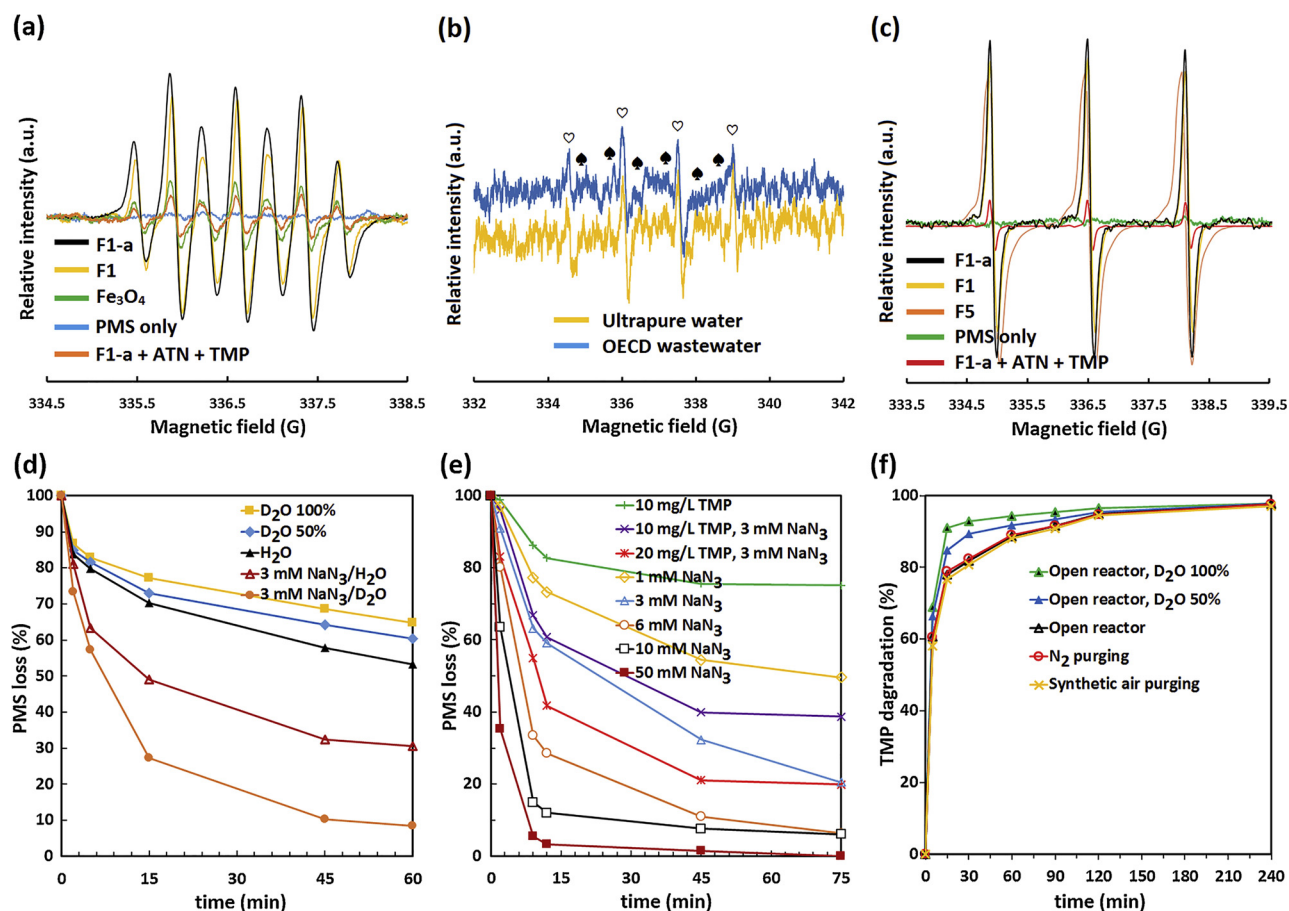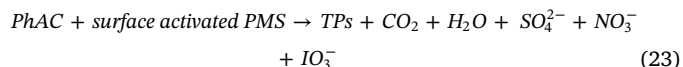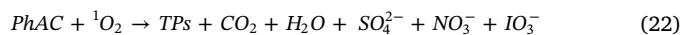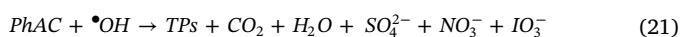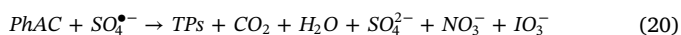**Fig. 9.** Detection of reactive oxygen species. Indicative EPR spectra of reactive oxidizers with DMPO (a,b) and TEMP (c). ([catalyst] = 0.05 g/L; [PMS]$_0$ = 0.2 g/L; [DMPO]$_0$ = [TEMP]$_0$ = 0.1 M; 25 ± 2 °C; contact time 15 min). ♠ ≡ DMPO-SO$_4^-$ and ♡ ≡ DMPO-OH; contact time 15 min). Validation of singlet oxygenation via solvent exchange effects on (d) PMS decay in the presence of azide (no catalyst), (e) PMS decomposition in the TMP@F1-a system with various azide concentrations and (f) Degradation efficiency of TMP under different atmospheres. ([F1-a] = 0.05 g/L; [PMS]$_0$ = 2 mM; native pH; 25 ± 2 °C).

acted as the main pathway followed by ˙OH attack. Surface-bound $SO_4^{•-}$ would also the critical for TMP decay over F1-a in these particular catalysis. However, many factors could affect the oxidant generation and product distribution: the nature of PhACs; the molar ratio between scavenger, PhAC and oxidant; the affinity of oxone to the carbofoam surfaces, solvents and the affinity of scavengers and PhACs to the activator surfaces; and the reactivity of the generated radicals with quenchers, PhACs and catalyst surfaces. For example, $SO_4^{•-}$ radical anion has relatively lower propensity for hydrogen abstraction than ˙OH, consequently may appear less critical in the identification of oxidation by-products of IOP (see 3.7. Identification of transformation products). The failure of highly concentrated scavengers to inhibit TMP removal could be partly explained by the contribution of other non-radical processes.

In Fig. 8c, sodium azide exerted less severe inhibition even at high molar excess (10 mM). Because azide reacts rapidly with PMS [10,19,68,72], the effect of $^1O_2$ scavenging needs to be validated. Solvent exchange (H_2O to D_2O) was first used to extend the lifetime of $^1O_2$ [87], aiming to endorse the potential role of $^1O_2$ (Fig. 9d). Without the presence of PhACs, the isotope-exchanged solvent induced less PMS decay. However, adding NaN_3 (3 mM) substantially accelerated the decomposition and D_2O likely stimulated the loss. These observations suggested that: (1) D_2O accelerated transferring the terminal peroxide oxygen to azide; (2) singlet oxygenation could be present and the activated-decomposition of PMS into $^1O_2$ was more favored as long as quenching reagent available. Like the other oxidants, $^1O_2$ would readily react with the contaminants of its selectivity range. Introducing azide (1–50 mM) accelerated PMS decomposition (Fig. 9e). Adding 3 mM NaN_3 to TMP@F1-a system initially boosted the decomposition of oxone but quickly attained plateau, which was in accordance with TMP removal rate (Fig. 8c). The oxidant decay appears to proceed further with higher concentrated TMP solution, although azide remained in excess. It is plausible that the activated-PMS conversion competed with those destruction initiated by azide. Thus, the observed quenching in Fig. 9c was likely due to both PMS ineffective losses and $^1O_2$ scavenging activity of azide. Indeed, within the first 60 min, the degradation efficiency arising for TMP over PMS@F1-a operated in 50% and 100% D_2O was ~14.5 and 25% kinetically higher than the performances in deionized water (Fig. 9f). These results supported that $^1O_2$ may actually have contributed to the carbocatalysis. In addition, negligible impacts of different reaction atmospheres suggested that oxone rather than dissolved oxygen in the reaction solution produced $^1O_2$. Despite $^1O_2$ can effectively react with conjugated double bonds and aromatics containing high electron density positions, the protonated ATN, MET and neutral IOP appear to be less susceptible. The relatively fast phenol decomposition at acidic pH (Fig. S7) might have ruled out the predominant role of $^1O_2$ in non-radical mechanism for phenol-like compounds or aromatics with electron-donating substituents. Conclusively, principal oxidation mediated by $^1O_2$ should not have a major implication on all PhACs under the studied experimental conditions.

Although PMS could oxidize azide to inert N_2 and N_2O, 23% of terminal peroxide oxygen of oxone was not transferred to the reductant while the generated highly active azidyl radical would also interact with substrates [88]. Therefore, the reactivities of PMS/azide and PMS@carbofoam/azide systems towards specific PhACs are difficult to rationalize, especially the roles of azidyl radical. Nevertheless, both radical (free and surface-bound) and non-radical (singlet oxygenation, mediated electron transfer) may all contributed to PhACs degradation, thus maintaining high decontamination efficiencies observed in different scenarios. The conversions that are pertinent for discussion of the oxidative degradations via dual-mode activation of PMS, as illustrated in Scheme 2, thus include:

$$PhAC + SO_4^{•-} \rightarrow TPs + CO_2 + H_2O + SO_4^{2-} + NO_3^- + IO_3^- \qquad (20)$$

$$PhAC + {}^•OH \rightarrow TPs + CO_2 + H_2O + SO_4^{2-} + NO_3^- + IO_3^- \qquad (21)$$

$$PhAC + {}^1O_2 \rightarrow TPs + CO_2 + H_2O + SO_4^{2-} + NO_3^- + IO_3^- \qquad (22)$$

$$PhAC + surface\ activated\ PMS \rightarrow TPs + CO_2 + H_2O + SO_4^{2-} + NO_3^-$$
$$+ IO_3^- \qquad (23)$$

3.5. Reactivity, structural stability and reusability of spent catalysts

Direct engineering carbofoams from p-SW allowed the retention the residual metallic proportion that offers magnetic-driven separation while preserving their potential synergistic catalytic effects. It was observed that after extensive sonication for 2 h, the magnetic separability of the catalysts was reduced in order: p-SW < F1 < F5, but remained excellent for F1-a and F5-a samples. Beside their higher performances, the good magnetic recyclability of the macroscopic carbofoams would facilitate its isolation and recovery in practical application. In addition, the macroscopic 3D architected structure would provide an ideal morphology for mass transfer, leading to less severe deterioration of active sites during the oxidation process. The interconnected glued foams would significantly eliminate secondary pollution (i.e. CNT leaching), which is highly desired in wastewater engineering nowadays. Indeed, the low leaching of nanotubes and the preservation of rapid magnetic isolations confirmed the robustness of coated-CNT scaffolds (Figs. S14). The coating layers may also improve the catalyst stability, lifetime, and recyclability. Reusability was thus evaluated in terms of cycle catalysis. Fig. 10 shows very encouraging performance with five consecutive reuses with almost complete degradation of ATN and TMP. The F1-a demonstrated slower kinetics but relatively similar degradation efficiencies within the studied timeframe of 2 h. The small lag between curves in the first hour indicated a deficiency of active sites after regenerations. The hybrids remained highly active for several cycles although possible active site coverage, defect detachment, and network breakdown appeared in the spent samples (Table 2, entry 8, 9). Graphitization changes were observed (Fig. 1c) with a reduction in Raman intensity and the I_G/I_D ratio was indicative of an abridged graphitic level and variation in defect density (Fig. 2d). The N content negligibly decreased in the regenerated F1-a, even though the graphitic-N/pyrrolic-N ratios declined markedly (Fig. S3). These results confirmed graphitized carbon as shielding 'skins' to protect surficial moieties and Me-N_x-C sites against substantial deactivation [6,28,42,65]. The performance drop thus mirrors the gradual detachment of active moieties, blocking of pores by intermediates, or oxidant overloading [7]. Nonetheless, materials regeneration by brief sonication was found sufficient, owing to its rich hierarchical porosity. Recovering of graphitic species on the passivated activator via heat treatment would also possible due to the high thermal stability of the carbofoams. Therefore, the foams were demonstrated to be very promising magnetic, durable and high-performance 3D carbocatalysts for degradation of PhACs due to its easy separation, facile recovery and subsequent reuses.

3.6. Identification of transformation products

The potential TPs resulting from the degradation of 20 mg/L PhACs using 1 g/L Oxone® after 5 and 120 min reaction were identified using the ESI FT-ICR MS technique. Full scan spectra were used to identify products with accurate m/z values and the proposed empirical chemical formulas as shown in Table S6. Deiodinations of iodine atoms from IOP were observed, whereas dimerization of ATN was unclear. The fragment with m/z 307, which indicates the direct attack of hydroxyl radical onto the benzene ring on TMP, was not observed, likely due to its fast transformation rate [49]. No zwitterionic intermediate of TMP was noted, suggesting the overall product distribution was mainly governed by radical attacks [49,50]. Although a complete disappearance of parent compounds was verified after 2 h, the presence of complex TPs retarded the complete mineralization of samples. Indeed, the most
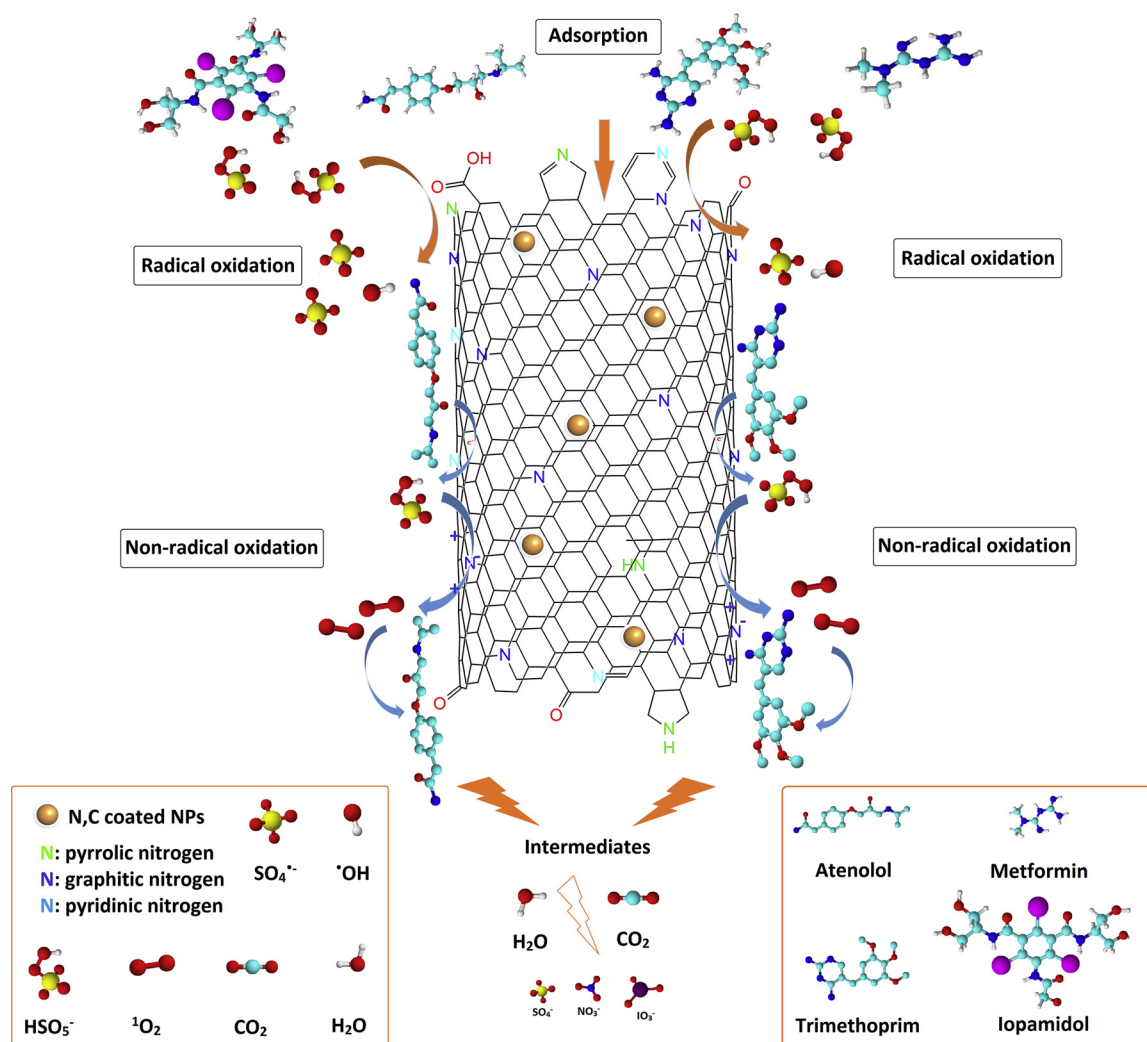
Scheme 2. Proposed degradation of PhACs via dual-mode activation of PMS on CNT foams.

promising non-purgeable organic carbon decay was observed for ATN (TOC$_{2h}$ = 2.58 mg/L corresponding to a 59% removal), while MET represented the lowest efficiency (TOC$_{2h}$ = 4.29 mg/L, 27% removal). The observation of smaller fragments indicated PhAC decay to simpler molecules. The observed TPs could be linked to the parent compounds via: electron transfer, electrophilic hydroxylation, oxidation of amine moieties, H-abstraction, decarboxylation and mixed reaction routes. Particularly, the TPs of TMP and IOP were also transformed via carbon-centered radical cations, which is initiated by sulfate radical-mediated electron transfer. From the product distribution profile, the hydroxyl radical-based oxidation of the aromatic ring and side chain was likely the dominant pathway [50,52–58].

The tentative degradation mechanisms for PhACs are proposed as shown in Schemes 3 and S1-3. In the case of IOP, 19 high-molecular weight transformation products were identified. IOP775, IOP773 are formed by H-abstraction from alcohol groups. Consecutive attachment of reducing hydrated electrons forms deiodinated products IOP651, IOP525, and IOP399. The observed TPs IOP667 and IOP557 are attributed to substitutions of hydroxyl to iodo sites. The produced singlet oxygen is contributed to the formation of ketones as in IOP775, IOP773, and IOP771 [52,55]. The observation of IOP649 suggests a fast combination of iodine elimination, H-abstraction, and the oxidation of secondary alcohol. Sequential amide hydrolysis, oxidation of amine moiety, and H-abstraction of IOP651 forms N^1,N^3-bis(1-hydroxy-3-oxopropan-2-yl)-2,4-diiodo-5-nitrobenzene-1,3-dicarboxamide (IOP605). Similarly, fragment 5-amino-N^1,N^3-bis(1,3-dihydroxypropan-2-yl)-2-

iodobenzene-1,3-dicarboxamide (IOP453) at the beginning of the catalysis process indicated a rapid deiodination and amide hydrolysis of IOP651 [56]. Besides non-genotoxic high-molecular weight TPs [80], iodoacetic acid (IOP185) which has mutagenic in bacteria and genotoxic in mammalian cells [89], was observed. Although iodoform (CHI$_3$) was not identified in this oxidation system, it has been detected and accounted for around 1.5% of total organic iodine generated in AOP of IOP [54]. In practical applications, the (eco)toxicological consequences of degradation process needs sufficient attention, which allows addressing the operational parameters for the optimal removal (concentration, toxic effects, and bioaccumulation potential) of the PhAC micropollutants and their derivatives [90].

4. Conclusion

Free-standing 3D heteroatom-enriched hierarchical porous foams were fabricated via direct carbonization and mild pyrolysis of renewable gingerbread ingredients on CNTs. Their catalytic performance in activating PMS for the degradation of pharmaceutical pollutants was found to be effective in various operating conditions. The synthesized carbofoams showed enhanced adsorption and oxidation potencies in comparison to pristine CNTs, Fe$_3$O$_4$ as well as chemically modified-activated carbon and cellulose nanocomposites. The un-annealed foams with high specific surface area and hierarchically structured heteroatom (N, O)-contained binding moieties were kinetically superior likely due to greater adsorptive sequestration, showing complete
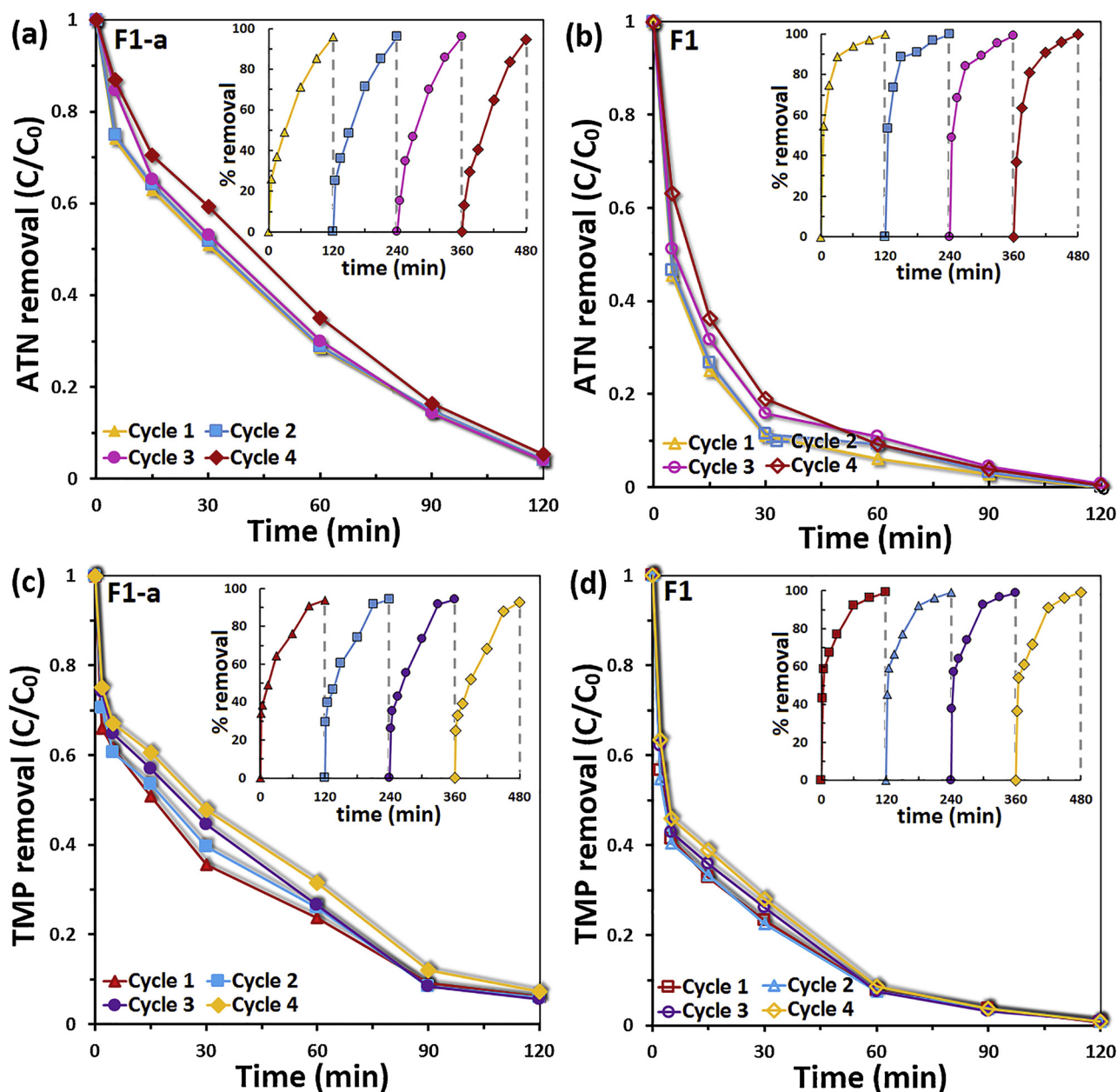
Fig. 10. Reusability of spent catalysts in PhACs degradation. Conditions: [PhAC] = 10 mg/L, native pH, unbuffered; [catalyst] = 0.1 g/L; [PMS]$_0$ = 1 g/L; 25 ± 2 °C.

removal of voluminous IOP within 15 min in the presence of PMS. The pronounced potency of the annealed carbofoams was attributed to the reactive carbonyl-O, graphitic-N active sites, surficial Me-N$_x$-C sites, and an enhanced electron transfer facilitated along the highly ordered graphitic framework. Studies on the impact of various operating parameters revealed that temperature, catalyst and PMS loading accelerated the removal efficiency, while tests in binary mixtures in different water matrices showed different inhibitory patterns. The carbofoams present stable 3D architecture, magnetic and catalytic stability, encouraging reusability and highly competitive potency with minor decay in activity, porosity, and magnetic-driven recovery. EPR, scavenging and solvent exchange study supported the involvement of $SO_4^{\bullet-}$, $^{\bullet}OH$, and $^1O_2$ via the dual-mode activation of PMS. FTICR-MS analysis suggested the formation of various transformation products, fulfilling tentative proposals of degradation pathways. Overall, this versatile renewable resources-based synthesis and shaped controllable magnetic marcosc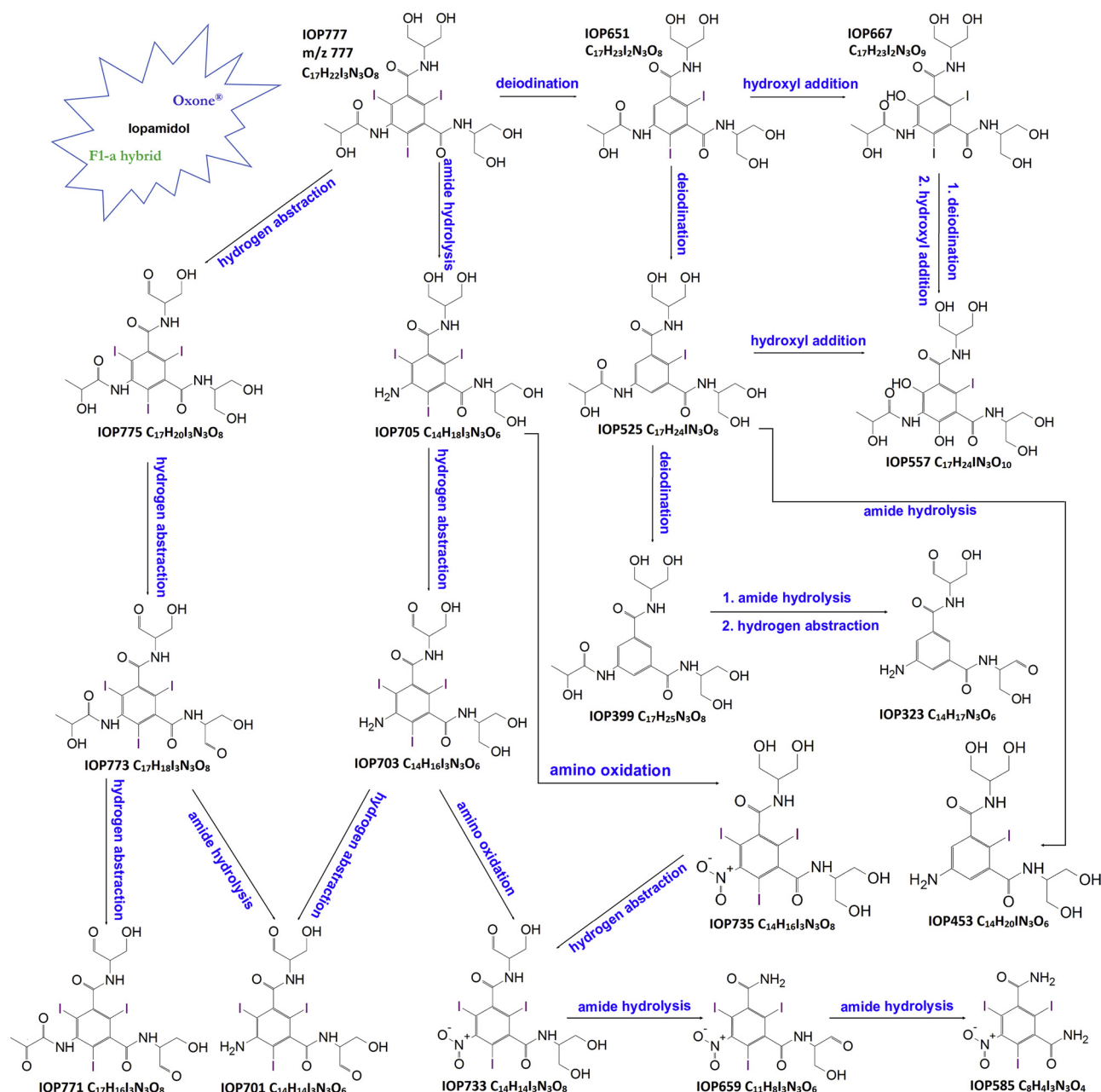opic carbocatalysts are highly expected to offer a promising alternative in remediating pharmaceutical-containing waters.

Appendix A. Supplementary data

Supplementary material related to this article can be found, in the online version, at doi:https://doi.org/10.1016/j.apcatb.2018.11.064.

Scheme 3. Proposed degradation pathways of IOP by F1-a@PMS oxidation.

References

[1] M.A. Shannon, P.W. Bohn, M. Elimelech, J.G. Georgiadis, B.J. Marinas, A.M. Mayes, Science and technology for water purification in the coming decades, Nature 452 (2008) 301–310.

[2] S.B. Grant, J.D. Saphores, D.L. Feldman, A.J. Hamilton, T.D. Fletcher, P.L.M. Cook, M. Stewardson, B.F. Sanders, L.A. Levin, R.F. Ambrose, A. Deletic, R. Brown, S.C. Jiang, D. Rosso, W.J. Cooper, I. Marusic, Taking the "waste" out of "wastewater" for human water security and ecosystem sustainability, Science 337 (2012) 681–686.

[3] J. Wilkinson, P.S. Hooda, J. Barker, S. Barton, J. Swinden, Occurrence, fate and transformation of emerging contaminants in water: an overarching review of the field, J. Env. Pol. 231 (2017) 954–970.

[4] A. Christou, A. Aguera, J.M. Bayona, E. Cytryn, V. Fotopoulos, D. Lambropoulou, C.M. Manaia, C. Michael, M. Revitt, P. Schroder, D.F. Kassinos, The potential implications of reclaimed wastewater reuse for irrigation on the agricultural environment: the knowns and unknowns of the fate of antibiotics and antibiotic resistant bacteria and resistance genes - A review, Water Res. 123 (2017) 448–467.

[5] D.S.S. Raghavan, G. Qiu, Y.P. Ting, Fate and removal of selected antibiotics in an osmotic membrane bioreactor, Chem. Eng. J. 334 (2018) 198–205.

[6] G.P. Anipsitakis, D.D. Dionysiou, Degradation of organic contaminants in water with sulfate radicals generated by the conjunction of peroxymonosulfate with cobalt, Environ. Sci. Technol. 37 (2003) 4790–4797.

[7] W.D. Oh, Z. Dong, T.T. Lim, Generation of sulfate radical through heterogeneous catalysis for organic contaminants removal: current development, challenges and prospects, Appl. Catal. B 194 (2016) 169–201.

[8] F. Ghanbari, M. Moradi, Application of peroxymonosulfate and its activation methods for degradation of environmental organic pollutants: review, Chem. Eng. J. 310 (2017) 41–62.

[9] J. Wang, S. Wang, Activation of persulfate (PS) and peroxymonosulfate (PMS) and application for the degradation of emerging contaminants, Chem. Eng. J. 334 (2018) 1502–1517.

[10] X. Duan, H. Sun, Z. Shao, S. Wang, Nonradical reactions in environmental remediation processes: uncertainty and challenges, Appl. Catal. B 224 (2018) 973–982.

[11] M. Klavarioti, D. Mantzavinos, D. Kassinos, Removal of residual pharmaceuticals from aqueous systems by advanced oxidation processes, Environ. Int. 35 (2009) 402–417.

[12] X.G. Duan, H.Q. Sun, Y.X. Wang, J. Kang, S.B. Wang, N-doping-induced nonradical reaction on single-walled carbon nanotubes for catalytic phenol oxidation, ACS Catal. 5 (2015) 553–559.

[13] H. Liu, P. Sun, M. Feng, H. Liu, S. Yang, L. Wang, Z. Wang, Nitrogen and sulfur co-doped CNT-COOH as an efficient metal-free catalyst for the degradation of UV filter BP-4 based on sulfate radicals, Appl. Catal. B 187 (2016) 1–10.

[14] Y. Yao, H. Chen, C. Lian, F. Wei, D. Zhang, G. Wu, B. Chen, S. Wang, Co Fe, Ni nanocrystals encapsulated in nitrogen-doped carbon nanotubes as Fenton-like catalysts for organic pollutant removal, J. Hazard. Mater. 314 (2016) 129–139.

[15] X. Pan, J. Chen, N. Wu, Y. Qi, X. Xu, J. Ge, X. Wang, C. Li, R. Qu, V.K. Sharma, Z. Wang, Degradation of aqueous 2,4,4'-Trihydroxybenzophenone by persulfate activated with nitrogen doped carbonaceous materials and the formation of dimer products, Wat. Res. 143 (2018) 176–187.

[16] Y. Yao, C. Lian, G. Wu, Y. Hu, F. Wei, M. Yu, S. Wang, Synthesis of "sea urchin"-like carbon nanotubes/porous carbon superstructures derived from waste biomass for treatment of various contaminants, Appl. Catal. B 219 (2017) 563–571.

[17] X. Duan, H. Sun, S. Wang, Metal-free carbocatalysis in advanced oxidation reactions, Acc. Chem. Res. 51 (2018) 678–687.

[18] W. Peng, S. Liu, H. Sun, Y. Yao, L. Zhi, S. Wang, Synthesis of porous reduced graphene oxide as metal-free carbon for adsorption and catalytic oxidation of organics in water, J. Mater. Chem. A Mater. Energy Sustain. 1 (19) (2013) 5854–5859.

[19] E.T. Yun, G.H. Moon, H. Lee, T.H. Jeon, C. Lee, W. Choi, J. Lee, Oxidation of organic pollutants by peroxymonosulfate activated with low-temperature-modified nanodiamonds: understanding the reaction kinetics and mechanism, Appl. Catal. B 237 (2018) 432–441.

[20] C. Wang, J. Kang, P. Liang, H. Zhang, H. Sun, M.O. Tadé, S. Wang, Ferric carbide nanocrystals encapsulated in nitrogen-doped carbon nanotubes as an outstanding environmental catalyst, Environ. Sci. Nano 4 (2017) 170–179.

[21] X.G. Duan, Z.M. Ao, L. Zhou, H.Q. Sun, G.X. Wang, S. Wang, Occurrence of radical and nonradical pathways from carbocatalysts for aqueous and nonaqueous catalytic oxidation, Appl. Catal. B 188 (2017) 98–105.

[22] X. Duan, K. O'Donnell, H. Sun, Y. Wang, S. Wang, Sulfur and nitrogen co-doped graphene for metal-free catalytic oxidation reactions, Small 11 (2015) 3036–3044.

[23] W. Tian, H. Zhang, X. Duan, H. Sun, M.O. Tade, H.M. Ang, S. Wang, Nitrogen- and sulfur-codoped hierarchically porous carbon for adsorptive and oxidative removal of pharmaceutical contaminants, ACS Appl. Mater. Interfaces 8 (2016) 7184–7193.

[24] X. Chen, W.D. Oh, Z.T. Hu, Y.M. Sun, R.D. Webster, S.Z. Li, T.T. Lim, Enhancing sulfacetamide degradation by peroxymonosulfate activation with N-doped graphene produced through delicately-controlled nitrogen functionalization via tweaking thermal annealing processes, Appl. Catal. B 225 (2018) 243–257.

[25] Y. Wang, Z. Ao, H. Sun, X.G. Duan, S. Wang, Activation of peroxymonosulfate by carbonaceous oxygen groups: experimental and density functional theory calculations, Appl. Catal. B 198 (2016) 295–302.

[26] J. Kang, X. Duan, C. Wang, H. Sun, X. Tan, M.O. Tade, S. Wang, Nitrogen-doped bamboo-like carbon nanotubes with Ni encapsulation for persulfate activation to remove emerging contaminants with excellent catalytic stability, Chem. Eng. J. 332 (2018) 398–408.

[27] S. Waclawek, H.V. Lutze, K. Grubel, V.V.T. Padil, M. Cernik, D.D. Dionysiou, Chemistry of persulfates in water and wastewater treatment: a review, Chem. Eng. J. 330 (2017) 44–62.

[28] P. Shao, J. Tian, F. Yang, X. Duan, S. Gao, W. Shi, X. Luo, F. Cui, S. Luo, S. Wang, Identification and regulation of active sites on nanodiamonds: Establishing a highly efficient catalytic system for oxidation of organic contaminants, Adv. Funct. Mater. 28 (2018) 1705295.

[29] R. Das, C.D. Vecitis, A. Schulze, B. Gao, A.F. Ismail, X. Lu, J. Chen, S. Ramakrishna, Recent advances in nanomaterials for water protection and monitoring, Chem. Soc. Rev. 46 (2017) 6946–7020.

[30] L. Canesi, C. Ciacci, T. Balbi, Interactive effects of nanoparticles with other contaminants in aquatic organisms: friend or foe? Marine Environ. Res. 111 (2015) 128–134.

[31] N. Kobayashi, H. Izumi, Y. Morimoto, Review of toxicity studies of carbon nanotubes, J. Occup. Health 59 (2017) 394–407.

[32] T. Chernova, F.A. Murphy, S. Galavotti, X.M. Sun, I.R. Powley, S. Grosso, A. Schinwald, J.Z. Cabeza, K.M. Dudek, D. Dinsdale, J.L. Quesne, J. Bennett, A. Nakas, P. Greaves, C.A. Poland, K. Donaldson, M. Bushell, A.E. Willis, M. MacFarlane, Long-fiber carbon nanotubes replicate asbestos-induced mesothelioma with disruption of the tumor suppressor gene Cdkn2a (Ink4a/Arf), Curr. Biol. 27 (2017) 3302–3314.

[33] R. Hjorth, L.M. Skjolding, S.N. Sorensen, A. Baun, Regulatory adequacy of aquatic ecotoxicity testing of nanomaterials, NanoImpact 8 (2017) 28–37.

[34] Y. Liu, H. Ba, D.L. Nguyen, O. Ersen, T. Romero, S. Zafeiratos, D. Begin, I. Janowska, C.P. Huu, Synthesis of porous carbon nanotubes foam composites with a high accessible surface area and tunable porosity, J. Mater. Chem. A Mater. Energy Sustain. 1 (2013) 9508–9516.

[35] K. Chizari, A. Deneuve, O. Ersen, I. Florea, Y. Liu, D. Edouard, I. Janowska, D. Begin, C.P. Huu, Nitrogen-doped carbon nanotubes as a highly active metal-free catalyst for selective oxidation, ChemSusChem 5 (2012) 102–108.

[36] H. Ba, Y. Liu, L.T. Phuoc, C.D. Viet, J.M. Nhut, D.L. Nguyen, O. Ersen, G. Tuci, G. Giambastiani, C.P. Huu, N-doped food-grade-derived 3D mesoporous foams as metal-free systems for catalysis, ACS Catal. 6 (2016) 1408–1419.

[37] H. Ba, J. Luo, Y. Liu, C.D. Viet, G. Tuci, G. Giambastiani, J.M. Nhut, L.N. Dinh, O. Ersen, D.S. Su, C.P. Huu, Macroscopically shaped monolith of nanodiamonds @ nitrogen-enriched mesoporous carbon decorated SiC as a superior metal-free catalyst for the styrene production, Appl. Catal. B 200 (2017) 343–350.

[38] H. Fei, Y. Wang, Z. Peng, G. Ruan, Q. Zhong, L. Li, E.L.G. Samuel, J.M. Tour, Cobalt nanoparticles embedded in nitrogen-doped carbon for the hydrogen evolution reaction, ACS Appl. Mater. Interfaces 7 (2015) 8083–8087.

[39] X. Zhang, M. Feng, L. Wang, R. Qu, Z. Wang, Catalytic degradation of 2-phenylbenzimidazole-5-sulfonic acid by peroxymonosulfate activated with nitrogen and sulfur co-doped CNTs-COOH loaded CuFe2O4, Chem. Eng. J. 307 (2017) 95–104.

[40] W. Ma, N. Wang, Y. Fan, T. Tong, X. Han, Y. Du, Non-radical-dominated catalytic

[41] degradation of bisphenol A by ZIF-67 derived nitrogen-doped carbon nanotubes frameworks in the presence of peroxymonosulfate, Chem. Eng. J. 336 (2018) 721–731.

[41] X.G. Duan, Z. Ao, H. Sun, L. Zhou, G. Wang, S. Wang, Insights into N-doping in single-walled carbon nanotubes for enhanced activation of superoxides: a mechanistic study, Chem. Commun. (Camb.) 51 (2015) 15249–15252.

[42] M. Qiao, S.S. Meysami, G.A. Ferrero, F. Xie, H. Meng, N. Grobert, M.M. Titirici, Low-cost chitosan-derived N-Doped carbons boost electrocatalytic activity of multiwall carbon nanotubes, Adv. Funct. Mater. 28 (2018) 1707284.

[43] Y. Zhang, L. Lu, S. Zhang, Z. Lv, D. Yang, J. Liu, Y. Chen, X. Tian, H. Jin, W. Song, Biomass chitosan derived cobalt/nitrogen doped carbon nanotubes for the electrocatalytic oxygen reduction reaction, J. Mater. Chem. A Mater. Energy Sustain. 6 (2018) 5740–5745.

[44] W. Seitz, W.H. Weber, J.Q. Jiang, B.J. Lloyd, M. Maier, D. Maier, W. Schulz, Monitoring of iodinated X-ray contrast media in surface water, Chemosphere 64 (2006) 1318–1324.

[45] M. Scheurer, A. Michel, H.J. Brauch, W. Ruck, F. Sacher, Occurrence and fate of the antidiabetic drug metformin and its metabolite guanylurea in the environment and during drinking water treatment, Water Res. 46 (2012) 4790–4802.

[46] Ingrid Bohm, Iodinated X-ray contrast media in aquatic environment in general and in drinking water in particular: a possible source for the primary sensitization of patients, Chemosphere 194 (2018) 28–29.

[47] X. Liu, T. Zhang, Y. Zhou, L. Fang, Y. Shao, Degradation of atenolol by UV/peroxymonosulfate: kinetics, effect of operating parameters and mechanism, Chemosphere 93 (2013) 2717–2724.

[48] G. Longobucco, L. Pasti, A. Molinari, N. Marchetti, S. Caramori, V. Cristino, R. Boaretto, C.A. Bignozzi, Photoelectrochemical mineralization of emerging contaminants at porous WO3 interfaces, Appl. Catal. B 204 (2017) 273–282.

[49] F.C. Moreira, R.A.R. Boaventura, E. Brillas, V.J.P. Vilar, Degradation of trimethoprim antibiotic by UVA photoelectro-Fenton process mediated by Fe (III)–carboxylate complexes, Appl. Catal. B 162 (2015) 34–44.

[50] Y. Ji, W. Xie, Y. Fan, Y. Shi, D. Kong, J. Lu, Degradation of trimethoprim by thermoactivated persulfate oxidation: reaction kinetics and transformation mechanisms, Chem. Eng. J. 286 (2016) 16–24.

[51] M. Neamtu, A. Grandjean, A. Sienkiewicz, S.L. Faucheur, V. Slaveykova, J.J.V. Colmenares, C. Pulgarin, L.F. de Alencastro, Degradation of eight relevant micropollutants in different water matrices by neutral photo-Fenton process under UV254 and simulated solar light irradiation – a comparative study, Appl. Catal. B 158-159 (2014) 30–37.

[52] J. Joonseon, J. Jung, W.J. Cooper, W. Song, Degradation mechanisms and kinetic studies for the treatment of X-ray contrast media compounds by advanced oxidation/reduction processes, Water Res. 44 (2010) 4391–4398.

[53] C. Zhao, L.E. Arroyo-Mora, A.P. DeCaprio, V.K. Sharma, D.D. Dionysiou, K.E. O'Shea, Reductive and oxidative degradation of iopamidol, iodinated X-ray contrast media, by Fe(III)-oxalate under UV and visible light treatment, Water Res. 67 (2014) 144–153.

[54] X. Duan, X. He, D. Wang, S.P. Mezyk, S.C. Otto, R.M. Vega, M.A. Mills, D.D. Dionysiou, Decomposition of iodinated pharmaceuticals by UV-254 nm-assisted advanced oxidation processes, J. Haz. Mater. 323 (2017) 489–499.

[55] J. Hu, H. Dong, J. Qu, Z. Qiang, Enhanced degradation of iopamidol by peroxymonosulfate catalyzed by two pipe corrosion products (CuO and δ-MnO2), Water Res. 112 (2017) 1–8.

[56] H. Liu, Q. Yu, H. Fu, Y. Wan, X. Qu, Z. Xu, D. Yin, S. Zheng, Pt supported on ordered microporous carbon as highly active catalyst for catalytic hydrodeiodination of iodinated X-ray contrast media, Appl. Catal. B 222 (2018) 167–175.

[57] H. Dong, Z. Qiang, S. Liu, J. Li, J. Yu, J. Qu, Oxidation of iopamidol with ferrate (Fe (VI)): kinetics and formation of toxic iodinated disinfection by-products, Water Res. 130 (2018) 200–207.

[58] M. Yan, Z. Chen, N. Li, Y. Zhou, C. Zhang, G. Korshin, Electrochemical reductive dehalogenation of iodine-containing contrast agent pharmaceuticals: examination of reactions of diatrizoate and iopamidol using the method of rotating ring-disc electrode (RRDE), Water Res. 136 (2018) 104–111.

[59] A.C. Alder, C. Schaffner, M. Majewsky, J. Klasmeier, K. Fenner, Fate of β-blocker human pharmaceuticals in surface water: comparison of measured and simulated concentrations in the Glatt Valley Watershed, Switzerland, Water Res. 44 (2010) 936–948.

[60] R.M. Briones, A.K. Sarmah, L.P. Padhye, A global perspective on the use, occurrence, fate and effects of anti-diabetic drug metformin in natural and engineered ecosystems, J. Env. Pol. 219 (2016) 1007–1020.

[61] Z. Xu, X. Li, X. Hu, D. Yin, Distribution and relevance of iodinated X-ray contrast media and iodinated trihalomethanes in an aquatic environment, Chemosphere 184 (2017) 253–260.

[62] B. Kolar, L. Arnus, B. Jeretin, A. Gutmaher, D. Drobne, M.K. Durjava, The toxic effect of oxytetracycline and trimethoprim in the aquatic environment, Chemosphere 115 (2014) 75–80.

[63] D. Armbruster, O. Happel, M. Scheurer, K. Harms, T.C. Schmidt, H.J. Brauch, Emerging nitrogenous disinfection byproducts: transformation of the antidiabetic drug metformin during chlorine disinfection of water, Water Res. 79 (2015) 104–118.

[64] C.H. Jeong, E.J. Machek, M. Shakeri, S.E. Duirk, T.A. Ternes, S.D. Richardson, E.D. Wagner, M.J. Plewa, The impact of iodinated X-ray contrast agents on formation and toxicity of disinfection by-products in drinking water, J. Env. Sci. 58 (2017) 173–182.

[65] M. Brienza, M.M. Ahmed, A. Escande, G. Plantard, L. Scrano, S. Chiron, S.A. Bufo, V. Goetz, Use of solar advanced oxidation processes for wastewater treatment: follow-up on degradation products, acute toxicity, genotoxicity and estrogenicity,

Chemosphere 148 (2016) 473–480.

[66] Y. Wang, H. Sun, X. Duan, H.M. Ang, M.O. Tade, S. Wang, A new magnetic nano zero-valent iron encapsulated in carbon spheres for oxidative degradation of phenol, Appl. Catal. B 172-173 (2015) 73–81.

[67] X. Duan, C. Su, L. Zhou, H.Q. Sun, A. Suvorova, T. Odedairo, Z.H. Zhu, Z.P. Shao, S.B. Wang, Surface controlled generation of reactive radicals from persulfate by carbocatalysis on nanodiamonds, Appl. Catal. B 194 (2016) 7–15.

[68] E.T. Yun, J.H. Lee, J. Kim, H.D. Park, J. Lee, Identifying the nonradical mechanism in the peroxymonosulfate activation process: singlet oxygenation versus mediated electron transfer, Environ. Sci. Technol. 52 (2018) 7032–7042.

[69] D. Li, X. Duan, H. Sun, J. Kang, H. Zhang, M.O. Tade, S. Wang, Facile synthesis of nitrogen-doped graphene via low-temperature pyrolysis: the effects of precursors and annealing ambience on metal-free catalytic oxidation, Carbon 115 (2017) 649–658.

[70] W. Tian, H. Zhang, Z. Qian, T. Ouyang, H. Sun, J. Qin, M.O. Tade, S. Wang, Bread-making synthesis of hierarchically Co@C nanoarchitecture in heteroatom doped porous carbons for oxidative degradation of emerging contaminants, Appl. Catal. B 225 (2018) 76–83.

[71] C. Liang, C.F. Huang, N. Mohanty, R.M. Kurakalva, A rapid spectrophotometric determination of persulfate anion in ISCO, Chemosphere 73 (2008) 1540–1543.

[72] Y. Yang, G. Banerjee, G.W. Brudvig, J.H. Kim, J.J. Pignatello, Oxidation of organic compounds in water by unactivated peroxymonosulfate, Environ. Sci. Technol. 52 (2018) 5911–5919.

[73] Y. Guo, Z. Zeng, Y. Zhu, Z. Huang, Y. Cui, J. Yang, Catalytic oxidation of aqueous organic contaminants by persulfate activated with sulfur-doped hierarchically porous carbon derived from thiophene, Appl. Catal. B 220 (2018) 635–644.

[74] F. Collin, H. Khoury, D.B. Rousselot, P. Therond, A. Legrand, D. Jore, M.G. Albert, Liquid chromatographic/electrospray ionization mass spectrometric identification of the oxidation end-products of metformin in aqueous solutions, J. Mass Spectrom. 39 (2004) 890–902.

[75] G. Boczkaj, A. Fernandes, Wastewater treatment by means of advanced oxidation processes at basic pH conditions: a review, Chem. Eng. J. 320 (2017) 608–633.

[76] C. Qi, X. Liu, J. Ma, C. Lin, X. Li, H. Zhang, Activation of peroxymonosulfate by base: implications for the degradation of organic pollutants, Chemosphere 151 (2016) 280–288.

[77] B. Hernandez, F. Pfluger, S.G. Kruglik, R. Cohen, M. Ghomi, Protonation-deprotonation and structural dynamics of antidiabetic drug metformin, J. Pharm. Biomed. Anal. 114 (2015) 42–48.

[78] Y. Yang, J.J. Pignatello, J. Ma, W.A. Mitch, Comparison of halide impacts on the efficiency of contaminant degradation by sulfate and hydroxyl radical-based advanced oxidation processes (AOPs), Environ. Sci. Technol. 48 (2014) 2344–2351.

[79] J. Choi, H. Lee, Y. Choi, S. Kim, S. Lee, S. Lee, W. Choi, J. Lee, Heterogeneous photocatalytic treatment of pharmaceutical micropollutants: effects of wastewater effluent matrix and catalyst modifications, Appl. Catal. B 147 (2014) 8–16.

[80] G.P. Anipsitakis, D.D. Dionysiou, M.A. Gonzalez, Cobalt-mediated activation of peroxymonosulfate and sulfate radical attack on phenolic compounds: implications of chloride ions, Environ. Sci. Technol. 40 (2006) 1000–1007.

[81] C. Liang, Z.-S. Wang, N. Mohanty, Influences of carbonate and chloride ions on persulfate oxidation of trichloroethylene at 20 °C, Sci. Total Environ. 370 (2006) 271–277.

[82] R. Yuan, S.N. Ramjaun, Z. Wang, J. Liu, Effects of chloride ion on degradation of Acid Orange 7 by sulfate radical-based advanced oxidation process: implications for formation of chlorinated aromatic compounds, J. Hazard Mat. 196 (2011) 173–179.

[83] F. Yang, Y. Huang, C. Fang, Y. Xue, L. Ai, J. Liu, Z. Wang, Peroxymonosulfate/base process in saline wastewater treatment: the fight between alkalinity and chloride ions, Chemosphere 199 (2018) 84–88.

[84] F.J. Rivas, R.R. Solis, Chloride promoted oxidation of tritosulfuron by peroxymonosulfate, Chem. Eng. J. 349 (2018) 728–736.

[85] S. Hou, L. Ling, D.D. Dionysiou, Y. Wang, J. Huang, K. Guo, X. Li, J. Fang, Chlorate formation mechanism in the presence of sulfate radical, chloride, bromide and natural organic matter, Environ. Sci. Technol. 52 (2018) 6317–6325.

[86] F.M. Wendel, T.A. Ternes, S.D. Richardson, S.E. Duirk, J.A. Pals, E.D. Wagner, M.J. Plewa, Comparative toxicity of high-molecular weight iopamidol disinfection byproducts, Environ. Sci. Technol. Lett. 3 (2016) 81–84.

[87] J.R. Hurst, J.D. McDonald, G.B. Schuster, Lifetime of singlet oxygen in solution directly determined by laser spectroscopy, J. Am. Chem. Soc. 104 (1982) 2065–2067.

[88] R.C. Thompson, P. Wieland, E.H. Appelman, Oxidation of azide and azidopentaamminechromium(III) by peroxymonosulfate in aqueous solution, Inorg. Chem. 18 (1979) 1974–1977.

[89] X. Wei, S. Wang, W. Zheng, X. Wang, X. Liu, S. Jiang, J. Pi, Y. Zheng, G. He, W. Qu, Drinking water disinfection byproduct iodoacetic acid induces tumorigenic transformation of NIH3T3 cells, Environ. Sci. Technol. 47 (2013) 5913–5920.

[90] Ursvon Gunten, Oxidation processes in water treatment: are we on track? Environ. Sci. Technol. 52 (2018) 5062–5075.